The Late Cenozoic tectonic evolution of Gurla Mandhata, Southwest Tibet

By

Andrew T. McCallister
B.S., University of Arizona, 2010

Submitted to the graduate degree program in Geology and the Graduate Faculty of the University of Kansas in partial fulfillment of the requirements for the degree of Master of Science.

_____

Chairperson: Michael H. Taylor

_____

Andreas Möller

_____

Leigh A. Stearns

_____

Daniel F. Stockli

Date Defended: October 10/10/2012

The Thesis Committee for Andrew T. McCallister
certifies that this is the approved version of the following thesis:

The Late Cenozoic tectonic evolution of Gurla Mandhata, Southwest Tibet

_____

Chairperson: Michael H. Taylor

Date approved: 12/3/1012

Abstract

How strain within the Tibetan plateau is geodynamically linked to that within the Himalayan thrust belt is a topic receiving considerable attention. The right-lateral Karakoram fault plays key roles in models describing the structural relationship between southern Tibet and the Himalaya. Considerable debate exists at the southeastern end of the Karakoram fault, where the role of the Karakoram fault is interpreted in two very different ways. One interpretation states that slip along the Karakoram fault extends eastward along the Indus-Yalu suture zone, thereby bypassing the Himalayan thrust belt to its north. The other, interprets that a significant component of the slip is fed southward into the Himalayan thrust belt along the Gurla Mandhata detachment. To evaluate this debate, the late Miocene fault slip rate history of the Gurla Mandhata detachment system is reconstructed from thermokinematic modeling with Pecube of zircon (U-Th)/He and biotite and muscovite $^{40}Ar/^{39}Ar$ thermochronometric ages. This slip rate history is then compared to that of the Karakoram fault. Zircon (U-Th)/He thermochronometric data from 3 east-west footwall transects reveal cooling of the Gurla Mandhata footwall through the zircon partial retention zone, from 8.01±1.31 Ma to 2.56±0.7 Ma. Results from ~21,100 Pecube models show a southward progression of decreasing fault slip magnitude and rate along the Gurla Mandhata detachment system. The northern transect modeling results show an initiation age from 14–11 Ma with a mean fault slip rate of 5.0±0.9 mm/yr. The central transect modeling results show an initiation age from 14–11 Ma with a mean fault slip rate of 3.3±0.6 mm/yr. The southern transect modeling results show an initiation age from 15-8 Ma with a mean fault slip rate of 3.2±1.6 Ma. These fault initiation ages and fault slip rate results match estimates obtained for the Karakoram fault across several timescales, supporting the idea that the two are kinematically linked. Specifically, the data are consistent with the Gurla Mandhata detachment

acting as a right-step extensional stepover along which the Karakoram fault slip is transferred into the Himalayan thrust belt of western Nepal.

Acknowledgments

This work was funded by the Tectonics Division of the National Science Foundation, and by the University of Kansas (Student Summer Scholarship). I would like to thank my advisor Michael Taylor for the guidance and support provided during the course of this project. I would also like to thank Andreas Möller, Danny Stockli, and Leigh Stearns for being on my committee. A large thanks is owed to Michael Murphy at the University of Houston, for without the samples, data, help, and guidance he provided this project would not have been possible. Additionally, thanks to Paul Kapp from the University of Arizona and Allex Pullen from Rochester University who provided samples to this project. I want to thank the Taylor group Richard Styron, Kurt Sundell, Gabriel Velosa, and Maureen Logan for their assistance and discussion that helped make this project what it is. Thank you to Roman Kislitsyn for the help and guidance in the lab. I would like to thank my lab mates Joe Miller, Josh Burrus, Sarah Evans, Josh Feldman, Bad'r Ghorbal, Jeff Oalmann, Willy Rittase, and Sam Coleman for their training, assistance, and discussions in the lab. Thanks to Tandis Bidgoli for all the great discussion and advice throughout the past two years. Also thank Richard Styron for his help with the PeCube modeling, and for his assistance and guidance in the field. Thank you to my family for the love and support during this adventure. Finally to Melissa McMillan, thank you for being my rock during the good and bad.

Table of Contents

(Page intentionally left blank)

(Page intentionally left blank)

The Late Cenozoic tectonic evolution of Gurla Mandhata, Southwest Tibet

1. Introduction:

The Tibetan plateau is one of the largest continental plateaus on Earth, with the final episode of collision initiating in the Early Cenozoic between the Indian and Eurasian plates [e.g. *Besse et al., 1984; Gaetani and Garzanti, 1991; Rowly, 1996; Zhu et al., 2005*]. Although the geology of the Tibetan plateau has been well studied, our understanding of the timing and mechanisms for regional kinematic fault motion are not well established. During the Early-Middle Miocene, there was a shift in the relative motion of southern Tibet and the northern Himalaya, from a system dominated by arc-normal shortening to one dominated by arc-parallel extension [*Mercier et al., 1987; Yin and Harrison, 2000*]. In the Himalaya and southern Tibet, the formation of arc-parallel structures exhumed mid-crustal rocks (Figure 1) such as the Ama Drime massif [*Jessup et al., 2008*], the Leo Pargil detachment [*Thiede et al., 2006*], and the Gurla Mandhata detachment [Murphy et al., 2002]. These faults accommodate regional kinematic changes and cross-cut older contractional structures. Arc-parallel extension in the Himalaya is contrary to expected fault patterns, as the Himalaya and southern Tibet are thought to accommodate north-south convergence. Thus, understanding this kinematic change is vital to understanding the dynamics of the Himalayan-Tibetan orogen.

Geologic documentation for the change from N-S contraction to E-W extension is observed in southern Tibet in the formation of large N-S striking normal faults, such as the Lopukangri [*Murphy et al., 2010*] North Lunggar [*Kapp et al., 2008*], Nyainqentanglha [*Pan and Kidd, 1992; Harrison et al., 1995; Kapp et al., 2005*], PumQu-Xainza, and Tangra Yum Co [*Dewane et al., 2006*] rifts. Geologic documentation is also found in central Tibet in the form of

large, east-striking, left and right slip faults, such as the Gyaring Co fault [*Tapponnier et al., 1981*], Riganpei Co fault [*Taylor et al., 2003*], and Jiali fault (Figure 1) [*Armijo et al., 1986*]. This cross-cutting relationship between active extensional structures and the older contractional structures has been previously reported [*Tapponnier et al., 1981; Harrison et al., 1995; Taylor et al., 2003; Taylor and Peltzer, 2006; Kapp et al., 2008; Murphy et al., 2010*]. In the Himalayas, the Gurla Mandhata, Ama Drime, Kungo Co, and Leo Pargil detachments also cut structures that previously accommodated north-south motions. Examples are the South Tibetan Detachment (STD) and the Main Central Thrust (MCT) [*Murphy et al., 2002; Murphy and Copeland, 2005; Thiede et al., 2006; Jessup et al., 2007, Lee et al., 2011*]. Although this shift in deformational style is well supported in the literature, the mechanisms and dynamics for such changes are not well understood.

By understanding the timing and kinematics of the Ama Drime, Leo Pargil, and Gurla Mandhata detachment systems, it may become possible to understand how the Tibetan plateau changed from a system dominated by arc-normal shortening to a system that now includes a significant component of arc-parallel extension. One step in understanding this change is examined in this thesis: the interactions between the Karakoram fault (KF) and the Gurla Mandhata detachment (GMD). These structures are relevant because previously proposed models for the kinematic change in Tibet and the Himalaya predict very specific interactions between the KF and GMD, which allows for comparison between the end-member models presented below.

1.1 Models for deformation of the Himalayan-Tibetan orogen

Numerous models attempt to explain how strain within the Tibetan plateau is geodynamically linked to that within the Himalayan thrust belt. The following four models are relevant to this study: oroclinal bending, radial spreading, oblique convergence, and lateral extrusion. It should be noted that there are two dominant groups of models: Himalayan-centric models and Tibetan-centric models. The Himalayan models may not specifically address fault development in Tibet and vice versa. For example, Himalayan models (oroclinal bending, radial spreading, and oblique convergence) do not specifically address the style of deformation seen in Tibet. The model-based predictions must be extrapolated to encompass southern Tibet for the Himalayan models, and vice versa, as this study is focused on the structural transition between the Himalaya and Tibet.

1.1.1 Oroclinal Bending

Oroclinal bending of a previously linear Himalayan arc arises from the collision between the Indian and the Eurasian continents. According to this model, the ends of the collision zone are folded inward in map pattern forming the eastern and western syntaxes (Figure 4B). This inward folding of the orogen induces sinistral motion along the KF, east-west directed normal faulting in the south central Himalaya, and dextral faulting near the eastern part of the Indus suture zone in Tibet [*Styron et al., 2011*]. Furthermore, implicit in the kinematics of oroclinal bending, E-W directed contractional strain occurs in central Tibet, potentially leading to the development of arc-normal oriented contractional structures. Evidence consistent with this model includes paleomagnetic rotations documented in the northwest Himalaya [*Klootwijk et al., 1985; Schill et al., 2001, 2002*], and arc-parallel faulting in the central Himalaya [*Ratschbacher et al., 1994; Li and Yin, 2008*]. However, the predicted kinematics for the KF, faults in central Tibet,

and southeastern Tibet do not match field observations. In particular, model predictions require sinistral motion on the KF, which are opposite to field observations of dextral faulting [*Ratschbacher et al., 1994; Searle et al., 1998; Murphy et al., 2000*].

1.1.2 Radial Spreading

Radial spreading of the Himalayan arc predicts that Tibetan crust is "flowing" outward from areas of high gravitational potential energy, outward and over its lower relief boundaries. The southeastern boundary of the plateau is not bound by strong, old crust and lithosphere, as seen on the western, eastern, and northern boundaries, allowing for lateral crustal flow at relatively high rates. This lateral flow is the result of high gravitational potential energy [*England and Houseman, 1988; Copley and McKenzie, 2007*] and hot crust capable of flow [*Bird, 1991; Beaumont et al., 2004*]. The resulting flow may lead to expansion of the southern boundary of the Himalaya increasing the circumference of the Himalayan arc [*Jade et al, 2004; Murphy and Copeland, 2005; Copely and McKenzie, 2007; Copley, 2008*] as well as the east-directed flow of material from central Tibet (Figure 4C). The radial spreading model also predicts arc-normal directed extension of southern Tibet and arc-parallel extension of the Himalaya as arc radius increases [*Ratsbacher et al., 1994; Styron et al., 2011*].

1.1.3 Oblique Convergence

Oblique convergence predicts that extension in the Himalaya and southern Tibet occurs primarily from the variation in oblique convergence of Indian plate relative to the arcuate Himalaya. This model suggests that the arc-parallel component of translation is commensurate with increasing convergence obliquity between India and the Himalaya. The resulting arc-

parallel component of extension is accommodated by arc-parallel strike-slip. Specifically, where convergence is perpendicular to the arc, extension will be dominantly accommodated by arc-normal striking normal faults. Moving along-strike from the central Himalaya, convergence obliquity increased, causing an increase in the arc-parallel extension component that is accommodated by arc-parallel strike slip faults. In summary, N-S striking normal faults are dominate in the central portion of the Himalaya and southern Tibet, while dextral motion along the Karakoram fault in the west, and sinstral motion along strike slip faults in the east are dominate (Figure 4D) [*McCaffrey and Nabelek, 1998; Seeber and Pecher, 1998; Styron et al. 2011*].

1.1.4 Lateral Extrusion

Lateral extrusion of Tibet predicts that blocks of central Tibetan crust are extruding eastward along plateau-bounding, strike-slip faults, thus accommodating the India-Eurasia collision. The sinistral Altyn Tagh fault bounding Tibet's northern boundary and the dextral KF and Indus-Yalu suture zone (IYS) along the southern boundary are thought to accommodate eastward motion of the central Tibetan crust (Figure 4A) [*Tapponnier et al., 1982; Tapponnier et al., 2001, Lacassin et al., 2004; Schill et al., 2004; Valli et al., 2007, 2008*]. This model predicts eastward rigid translation of Tibet, thus requiring minimal internal deformation. Faults are predicted by this model to have high slip rates and slip magnitude in Tibet. Faulting in the Himalayas, south of the IYS, is not explained by the lateral extrusion model. Furthermore, the diffuse nature of faulting in central Tibet would be considered negligible in the overall strain budget within Tibetan crust.

1.2 End-Member Models:

To identify the most predictive end-member models for Tibetan extension, the four models described above are grouped based on their fault predictions for southwest Tibet. The first set of models includes the oroclinal bending, the radial spreading, and the oblique convergence models. We choose to exclude the Oroclinal Bending model because it maintains that the KF is a sinstral strike-slip fault interacting with the GMD, but mapping of the fault has shown it to be a dextral strike-slip fault [*Armijo et al., 1989; Yin et al., 1999; Murphy et al., 2000; Robinson, 2009*]. We also feel that the Radial Spreading model is less favorable because GPS data [*Gan et al., 2007*] for southwestern Tibet show an increasing arc-parallel component towards the west [*Styron et al., 2010*]. This is inconsistent to what the Radial Spreading model predicts, which predicts that the arc-parallel component should remain constant across the length of the arc. Although we can not fully exclude the radial spreading model, we feel that the oblique convergence model is the most valid of the first-group models.

The second end-member model is the lateral extrusion model, which was originally proposed by *Tapponnier et al.* [*1982, 2001*]. This model predicts a distinctly different interaction of faults in southern Tibet and the Himalaya, with particular emphasis on the KF, the GMD, and the IYS (Figure 5). These fault predictions make the lateral extrusion model the most relevant of the second group to test for this study, which we outline in more detail below.

1.2.1 Specific Model Predictions

The two selected end-member models predict distinct interactions among the KF, GMD and IYS. The oblique convergence model predicts that slip transferred along the KF diverges from the IYS and is transferred instead across the GMD and south into the High Himalaya via

the Humla fault (Figure 5A). Implicit in this fault interaction is that the GMD acts as a right-step extensional structure within the KF system. Conversely, the lateral extrusion model predicts that slip from the KF continues eastward into and along the IYS zone, bypassing the GMD (Figure 5B). To evaluate the validity of these end-member models, the slip rates and initiation of the GMD are compared to the rates and magnitudes of fault slip for the KF.

The comparison of long term geologic fault slip rates will determine which end-member model is more appropriate. If the oblique convergence model is correct, the observed slip rates for the KF should be comparable to fault slip rates for the GMD. This requires that nearly all of the fault-slip on the KF is transferred to the GMD, and that the KF does not feed slip into the IYS zone. Conversely, if the lateral extrusion model is correct, then slip rates for the KF should be greater than those of the GMD, and that this kinematic relationship suggests that the KF transfers slip into and along the IYS zone.

2. Geology:

2.1 Geologic Setting:

The Tibetan Plateau is the largest and highest plateau on Earth. It is roughly 1,800 km wide and 800 km long with a mean elevation of +4000 m. This striking geologic feature is comprised of three terrains: Songpan-Ganzi, Qiangtang, and Lhasa. Each terrain is separated from its neighbor by a suture zone (Figure 1). These are known as the Jinsha Suture, Bangong-Nujiang Suture, and Indus-Yalu Suture. All observed and active structures on the plateau are either north-south striking normal faults [*Armijo 1986; Yin et al., 1999; Yin and Harrison, 2000*] or east-west striking strike slip faults [*Armijo, 1989; Taylor et al., 2003; Taylor et al., 2009*]. In Tibet, the strike-slip faults are located mainly along the Bangong-Nujiang suture, while normal

fault systems cut across the Lhasa terrain striking N-S and cut locally into the Himalaya (e.g., Ama Drime, Yadong-Gulu Rift) (Figure 1). Northern faults in the Qiangtang terrain are not as long, and the strike-slip faulting is more pervasive (i.e., more closely spaced) [*Taylor et al., 2003*].

The Himalaya is classically differentiated from the Tibetan Plateau because the rocks are solely derived from the Tethys Ocean and the Indian Craton [*Searle, 1986; Gaetani and Garzanti, 1991; Brookfield, 1993*]. This orogen is considered the highest on earth and contains a large majority of the +8000 m peaks. The Himalaya has an arc length of +2,000 km, rising from ~200 m up to +8000 m (highest point is Mount Everest at 8,846 m). The Himalaya is an active thrust-wedge comprising a series of south-directed thrusts (e.g., from south-north: the Main Boundary Thrust, the Main Frontal Thrust, and the Main Central Thrust) [*Murphy and Yin, 2003*] and a north-directed thrust (Great Counter Thrust) (Figure 3) [*Yin et al., 1999*].

The Himalayan rocks are broken down into three general packages: the Tethyan Sedimentary Sequence, the Greater Himalayan Sequence, and the Lesser Himalayan Sequence (Figure 3). The Tethyan Sedimentary Sequence is an Indian passive margin sequence that was accreted onto Eurasia during the closure of the Tethys Ocean ~60 Ma ago [*Murphy and Yin, 2003, Yin et al., 1999*], was deformed by a thin-skinned thrusting during the Early Oligocene to Middle Miocene [*Murphy and Yin, 2003*], and is bounded by the South Tibetan Detachment (STD) and the Great Counter Thrust (GCT) (Figure 3) [*Murphy and Yin, 2003; Yin et al., 1999; Ratschbacher et al., 1994, Heim and Gansser, 1939*]. Structurally, the Greater Himalayan Sequence lies below the Tethyan Sequence and is Precambrian in age [*DeCelles et al., 1998*]. It is composed of deformed gneisses and paragneisses with extensive leucogranite intrusions [*DeCelles et al., 1998; Murphy and Yin, 2003*] and is bounded by the Main Central Thrust

(MCT) and the South Tibetan Detachment (STD) (Figure 3) [*Murphy and Yin, 2003; Burchfield et al., 1992; Burge and Chen, 1984*]. The lowest unit in the Himalaya is the Lesser Himalayan Sequence, which was formed sometime during the Early Miocene or Precambrian period [*DeCelles et al., 1998*]. These formations are composed of limestone, phyllite, gneisses, and schist [*Murphy et al., 2003*]. The Lesser Himalayan Sequence is bounded by the Main Boundary Thrust (MBT) and the Main Central Thrust (MCT) (Figure 3) [*Murphy et al., 2003; DeCelles et al., 2000; Brookfield, 1993; Parish and Hodges, 1996*].

The KF and the IYS zone are two structures which play important roles in models explaining the tectonic evolution of the Tibet-Himalayan orogeny. The dextral KF broadly coincides with the western boundary of the Tibetan plateau, from the Pamirs in the north to the Mt. Kailas region in the south (Figure 2). Previous work has shown that the KF is a southeast-striking dextral fault with ~149-167 km of offset in the northern portion biased on reconstructions of the Aghil formation [*Robinson et al., 2009*]. In the central section some authors have argued for 280-400 km of offset based on the reconstruction of the large opholitic packages [*Lacassin et al., 2004*]. Recent geochronologic work by *Wang et al.,* [*2012*] contradict the notion of 280-400 km of offset. Other authors have argued for ~120 km of slip at its central section [*Searle et al., 1998*]. At the southern section of the KF, ~65 km of slip is estimated based on reconstruction of the south Kailas thrust system [*Murphy et al., 2000*] and 35-50 km based on reconstruction of the Gar basin [Sanchez et al., 2010]. The central segment of the KF initiated ~16 Ma ago [*Searle et al., 1998*] and propagated southward, where it offset the south Kailas thrust ~13 Ma ago [*Yin et al., 1999; Murphy et al., 2000; Yin et al., 2000*]. This study focuses on the southern portion of the KF where debate exists on the kinematic interplay between the KF, and the Xiao Gurla segment of the GMD (Figures 2, 6).

The IYS zone locally marks the boundary between the Lhasa terrane and the Tethyan Himalaya (Figure 1). Where mapped, the IYS zone is delineated by the north-directed Great Counter Thrust [*Yin et al., 1999; Murphy et al., 2009; 2010; Sanchez et al., 2012*]. The IYS developed from the collision between the Indian and Eurasian plates.

2.2 Geology of Gurla Mandhata:

The Gurla Mandhata detachment lies south of the IYS zone (Figure 2). *Murphy et al.* [*2002*] provides the first description of this fault, observing it to be a series of west-dipping, moderate- to low-angle (22-45°) normal faults bounding the western and northern flanks of the Gurla Mandhata massif. Estimates of fault slip range between 35-66 km for the area along the northern and central sections of the fault [*Murphy et al., 2002*] and ~35 km of slip along the southern section of the massif [*Murphy and Copeland 2005*]. $^{40}Ar/^{39}Ar$ geochronology is consistent with exhumation of its footwall ca. 9 Ma ago [*Murphy et al., 2002; Murphy and Copeland, 2005*].

A series of en echelon normal faults cut the Pulan Basin, located in the immediate hanging wall of the GMD. These faults are primarily located on the eastern side of the Pulan basin (Figure 6), but previous studies have locally observed recently active faults along the western boundary [*Murphy et al., 2002; Murphy and Copeland, 2005, Murphy and Burgess, 2006; Chevalier et al., 2012*]. The active, west-dipping, high-angle normal faults have a mean slip direction of 274°$\pm$ 10° and a maximum throw of 200 m based on reconstructing offset Miocene-Pliocene sedimentary rocks [*Murphy et al., 2002*]. The high angle faults are thought to sole into the Gurla Mandhata detachment system at depth (Figure 7A). At the southernmost

segment of these high-angle faults, the GMD swings eastward, where it transfers slip into the dextral Humla Fault (Figure 6).

2.3 Lithologic Units

The hanging wall of the GMD is composed of 8 units - these include: (1) Kiogar Ophiolites (op), (2) Tethyan sequence (ts) rocks, (3) Cretaceous-Tertiary volcanic rocks (K-Tv), (4) Cretaceous-Tertiary granite (K-T), (5) Kailas sequence (ks) rocks, (6) Mesozoic group (Mv) rocks, (7) Pulan Basin strata (Tcg), and (8) Pulan basin Quaternary alluvium (Qtr). The footwall of the GMD is comprised of 5 units - these include: (1) Migmatite (mig), (2) gneiss (gn), (3) Greater Himalayan sequence (ghs) rocks, (4) Xiao Gurla sequence (xg) rocks, and (5) Leucogranite (gr).

2.3.1 Hanging Wall Units

The Kiogar Ophiolite sequence (op) is the oldest unit within the hanging wall rocks. The ophilitic rocks are mainly composed of norite, dunnite, and harzburgite [*Miller et al., 1999; Murphy et al., 2002*]. Tethyan sequence (ts) is exposed in the western edge of the field area and is a > 9 km-thick section of Upper Proterozoic through Lower Cretaceous sandstone, shale and limestone [*Murphy and Yin, 2003*]. This sequence is repeated by a series of north-dipping thrust faults. (Figure 6).

The Pulan basin strata are separated into two sequences: the older Pulan basin sediments (Tcg) and the younger Pulan basin sediments (Qtr). The older Pulan basin strata (Tcg) are composed of sandstones, shales, and conglomerates confined mainly to the southern half of the

Pulan basin [*Murphy et al., 2002*]. The younger strata (Qtr) are composed of clasts derived mainly from the footwall of the Gurla Mandhata detachment fault (Figure 6) [*Murphy et al., 2002*].

2.3.2 Footwall Units

Migmatitic gneiss (mig) is the structurally lowest unit in the footwall of the GMD (Figure 7). The rocks that make up the migmatite are banded gneisses with biotite-rich layers, and numerous leucosomes. A penetrative mylonitic fabric with the same shear sense as the GMD are observed throughout the unit [*Murphy et al., 2002*]. Geochemical analysis by *Murphy,* [*2007*] found that Nd and Sr isotope ratios of portions of the migmatite are consistent with a Lesser Himalayan sequence (lhs) protolith.

Above the migmatitic gneiss (mig) are quartzofeldspathic gneisses and biotite schists (gn) (Figure 7) [*Murphy et al., 2002*]. Penetrative ductile shear fabrics within these rocks are consistent with top-to-the-west shear sense (280 $\pm$ 4°) [*Murphy et al., 2002*]. Leucogranite dikes intrude the gneiss (gn), the dikes are sheared with the same top-to-the-west shear sense as the ductile fabrics. Cross-cutting relationships and shear sense indicators show that the dikes were likely emplaced during simple shear [*Murphy et al., 2002*]. Geochemical analyses indicate the gneisses have the same Nd and Sr isotopic signature as the Greater Himalayan sequence (ghs) [*Murphy, 2007*].

The Greater Himalayan sequence (ghs) makes up the structurally highest unit of the Gurla Mandhata massif (Figure 7) The majority of these rocks are highly deformed marbles and schists with top-to-the-west shear sense, along with extensive leucogranite intrusions also displaying the same shear sense, suggesting synkinematic emplacement [*Murphy et al., 2002*].

The Xiao Gurla sequence (xg) is composed of metamorphosed Tethyan sedimentary sequence (ts) rocks. Detrital U/Pb zircon analysis shows the Xiao Gurla sequence (xg) has the same detrital signature and lithology as the local Tethyan sedimentary sequence (ts) [*Pullen et al., 2011*]. Leucogranite dikes similar to the Gurla Mandhata footwall also intrude the Tethyan rocks.

The leucogranite (gr) dikes compose the youngest footwall unit. This unit makes up 10-20% of the footwall and intrudes all of the footwall units [*Murphy et al., 2002; Murphy and Copeland, 2005; Pullen et al., 2011*]. It is most commonly observed as 2-m thick dikes and sills with a similar sense of shear as the main faulting direction (top to the west), which is consistent with synkinematic emplacement [*Murphy et al., 2002; Murphy and Copeland, 2005; Pullen et al., 2011*]. *Pullen et al.* [*2011*] dated seven zircons from the footwall of the GMD, with a mean U-Pb age of 18.6 ± 0.9 Ma, along with seven zircon grains from the Xiao Gurla leucogranite sequence yielding an average U/Pb age of 19.5 ± 1.5 Ma. These samples are indistinguishable within error. They have crystallization ages older than the initiation age of the GMD of about 12 Ma [*Murphy et al., 2002*], suggesting that intrusion may be coeval with deformation and also predate deformation [*Murphy et al., 2002; Murphy and Copeland, 2005; Pullen et al., 2011*].

3. Methods

3.1 Zircon (U-Th)/He Thermochronology

(U-Th)/He low-temperature thermochronometry is a well-established technique for examining the cooling history of exhumed footwalls of normal faults [*Stockli, 2005*]. The strength of this technique lies in is its ability to assess the timing and rate of faulting, and is based on the alpha decay of ^{235}U, ^{238}U, and ^{232}Th [*Stockli, 2005*]. Alpha (^{4}He nuclide) retention in minerals is temperature dependent, and individual minerals have unique thermal sensitivity

windows called partial retention zones [*Stockli, 2005*]. For this study, we use zircon because it is relatively abundant in the footwall rock, and it has a partial retention zone that can track upper crustal processes between 175-190 °C (Figure 9) [*Reiners, 2005; Stockli, 2005*]. The samples analyzed here are described based on their relationship to the three transects described beginning in section 3.1.3.

3.1.1 Sample Processing

All samples were processed at the University of Kansas, Isotope Geochemistry Laboratory (IGL) using standard mineral separation techniques. For each sample, 3-8 zircon grains were analyzed using the methods described in *Wolfe and Stockli* [*2010*]. Individual zircon grains were packed in platinum packets and degassed under high-vacuum conditions. The degassed grains were removed from the platinum packets, dissolved, and the concentrations of the He parent isotopes of U, Th, and Sm were determined by isotope dilution on a Thermo Scientific Element 2 inductively coupled plasma mass-spectrometer (ICP-MS).

3.1.2 Samples

Samples were collected along three footwall transects subparallel to the slip direction of the GMD (Figure 6). Each transect is between 25-35 km in length across the footwall, with a 500-1000 m mean elevation change, and consists of 3-10 bedrock samples. Below we describe each transect from north to south.

3.1.3 Northern Transect

The northern transect consists of three (U-Th)/He thermochronometric samples collected along the Namarodi Valley northeast of the Gurla Mandhata peak. The data are combined with previously published thermochronometry data from the Ronggua Gorge (Figure 6). Two of the three samples were collected along the valley walls from exposed bedrock, while the third sample was collected from a ridge just east of the main valley (Figure 6). A mean elevation gain of ~500 m separates the lowest sample from the highest (A-A'; Figure 7A). We include two muscovite samples (Ar^{39}/Ar^{40} cooling ages), one biotite sample (Ar^{39}/Ar^{40} cooling age), all of which are from the Ronggua Gorge, and two biotite samples (Ar^{39}/Ar^{40} cooling age) from the Namarodi Valley [*Murphy et al., 2002*] in our modeling analysis in section 4.2.

3.1.4 Central Transect

The central transect is 35 km long and starts at the southern extent of the Pulan Basin (corresponding with cross-section B-B', Figure 7B) and continues up the Karnali tributary to the northeast into the core of the range (Figure 6). Thermochronometric samples were collected along the river valley floor or along the valley wall from exposed bedrock and spans ~ 700 m in elevation change. Ten samples were collected from the transect, representing all four of the footwall units (Table 1).

3.1.5 Southern Transect

The southern transect starts in the Karnali River valley close to the northwest termination of the Humla Fault, corresponding with cross-section C-C' (Figure 7C). The sample transect continues to the northeast, up a tributary gaining ~800 m in elevation and comprises eight samples from three of the four footwall units (Table 1).

3.1.6 Results

For this study, 21 samples were analyzed (3-7 aliquots each), with weighted averaged ages ranging from 2.6 ± 0.7 to 8.0 ± 1.3 Ma (Table 1). The sample transects demonstrate that (U-Th)/He ages become progressively older eastward into the footwall and with an increase in elevation (Figure 7). The northern transect is represented by three samples with a minimum age of 6.1 ± 0.8 Ma and a maximum age of 7.2 ± 1.2 Ma. The sample ages increase with elevation. The central transect is represented by 10 samples (3-7 aliquots) ranging in age from 4.5 ± 1.1 Ma to 8.0 ± 1.3 Ma. The age of the samples increase gradually into the GMD footwall and with increasing elevation (Table 1). The southern transect is represented by eight samples (4-5 aliquots) ranging from 2.6 ± 0.7 Ma to 4.2 ± 0.8 Ma in age, with the sample age increasing with elevation.

Comparing the three sample transects reveals an overall decrease in age to the south. This could be explained by a sampling bias, as the northern and southern transects do not intersect with the range front. Potential bias aside, with the exception of the last sample in the central transect, the oldest age for each transect youngs southward. At the eastern end of the central transect there is a small age jump from 6.5 Ma to 8.0 Ma (Figure 7B, Table 1). This increase is not due to a large elevation gain, suggesting a possible structural control. The proximity of the samples to a normal fault can well explain the juxtaposition of ages (Figure 6, 7). In addition to this trend, the extremely young ages across the entirety of the range suggest that the range must have been exhumed quickly over most of its development. Although there are extensive intrusions throughout the Gurla Mandhata range [*Murphy et al., 2002, Murphy and Copeland, 2005*] and nearby ranges [*Pullen et al., 2011*], published zircon U-Pb crystallization ages for the

GMD and nearby ranges are consistent with granitic intrusions emplaced prior to 18 Ma [*Pullen et al., 2011*].

4. Thermokinematic Modeling

In order to evaluate fault initiation, fault slip rate, and duration, we conducted thermokinematic modeling of our low temperature thermochronologic data from the GMD footwall rocks. Because the sampling transects across the GMD are horizontal and no samples have more then one thermochronometric age, conventional modeling software such as HeFTy or HeMP would be insufficient to determine the cooling history of the GMD. For this reason the data for the GMD are modeled in the finite element software package Pecube.

4.1 Pecube:

The zircon (U-Th)/He data were modeled using Pecube finite element software [*Braun, 2003*]. Pecube's ability to incorporate internal heating, isotherm advection, and a wide variety of thermochronometers [*Braun, 2003*] makes it an ideal modeling tool to investigate the late Cenozoic development of the GMD. Due to the spatial range of samples and the variability of the fault plane geometry, the data were modeled for each individual transect (Figure 9). Oriented in the slip direction, the data are ordered as follows: (1) the northern transect, located in the Ronggua Gorge, is composed of two $^{40}Ar/^{39}Ar$ muscovite and three $^{40}Ar/^{39}Ar$ biotite ages (as published by *Murphy et al.,* [2002]) and represented by four zircon (U-Th)/He samples (composing a vertical transect) (Figure 7A); (2) the central transect, represented by 15 zircon (U-Th)/He samples (Figure 7B); and (3) the southern transect, located at the inferred intersection of the Humla fault with the GMD, which is includes eight zircon (U-Th)/He samples (Figure 7C).

For all transects, the model space is oriented parallel to the average-slip direction (100°) (Figure 11) to better model the path that the samples would have traveled. The Moho depth is 65 km [*Nabelek et al., 2009; Chen et al., 2010*], as estimated by seismic Hi-Climb transects, with a base temperature of 800° C [*Nabelek et al., 2010; Nabelek and Nabelek, 2011*]. The internal heating value of 10 °C/My is based on radiogenic heat production [*Faccenda et al., 2008*]. The fault geometry is based on cross-sections presented in *Murphy et al.* [*2002*]. For the northern and central transects the model is allowed to initiate between 18-9 Ma, based on work by *Murphy et al.,* [*2002*], with a fault slip rate between 1-12 mm/yr. For the southern transect, the model is allowed to initiate between 15-7Ma, based on work by *Murphy and Copeland,* [*2005*], with a fault slip rate of 1-12 mm/yr. To better model the faults, all three transects are allowed to change slip rates once between 14-0Ma to rates between 0-12 mm/yr.

Several potential issues arise from complications within the fault system and computational limitations within Pecube: (1) The fault geometry of the GMD is complex and variable. In order to reconcile this complication, we use the mean fault dip for the corresponding fault segment. (2) Limitations within Pecube prevent any change in fault geometry during faulting. For this reason, we are limited to a static fault geometry as observed at the surface and the structural response of the hanging wall [*Murphy et al., 2002; Murphy and Copeland, 2005*]. (3) Because all faults within the Pecube model have the same strike and strike-length, any potential influence of the Humla Fault along the southern segment cannot be investigated. (4) Pecube limitations require all fault slip to be either normal or thrust, causing any strike-slip component to be negated. (5) Topography is considered to be steady state. Although these limitations are not specifically addressed in this work, we believe the modeling using Pecube is nonetheless sufficient to capture the Neogene thermal evolution of the GMD footwall.

4.2 Northern Transect

The northern transect corresponds to cross-section A-A' (Figure 7A). The model space extends well beyond the sample locations to avoid edge effects. The model is oriented to 280°, which is the general fault slip direction [*Murphy et al., 2002; Murphy and Copeland 2005*]. The fault strikes 010° with west dip of 30°. The shape of the fault plane is depicted in Figure 12. Early testing of model parameters show that a curved geometry projected above the surface is needed to reproduce the observed age-elevation trend. The domal fault geometry is also constrained by field observations, and fault-traces bounding the large triangular facets are observed on the entire western flank of the range (Figure 8B). The domal geometry of the footwall is also observed on other large extensional systems in Tibet [e.g. *Robinson et al., 2010; Styron et al., in review*].

Based on these initial model parameters, a total of 12,000 models were possible, each with a unique combination of fault history parameters. This set of possibilities was filtered using a resolvable range of possible slip magnitude values (14-62 km), based on field relationships and cross-section reconstructions [*Murphy et al., 2002*], described by *Styron et al.,* [*in review*]. This filtering reduced the total number of possible runs to ~6,700 models. (See Table 2 for model parameters.) These initial models were then run on Pecube v.3, in parallel on Amazon's EC2 servers through the PiCloud service (Picloud.com). See *Styron et al.,* [in review] for modeling workflow and Python codes. The initial results show that 45 of 6,700 models fit 4 out of 7 data points, and 2 of 6,700 models fit 5 out of 7 data points. No models were able to reproduces all 10 data points. None of the models were able to reproduce the GM-12 muscovite age within 2-σ (Figure 13A), and most of the modeled ages were found to be younger than GM-12. About a

third (34%) of the models were able to reproduce the sample GM-12 biotite age (Figure 13A). Only 23% of the models were able to reproduce sample HUM02-15 within 2-σ.

Possible initiation ages for faulting range between 9–16 Ma, with a mean of 11 Ma and a mode of 9 Ma (dark gray; Figure 14A). A large percentage of these models (81%) predict fault initiation between 9–12 Ma with a small percentage (19%) predicting an older fault initiation age between 13–16 Ma.

The initial fault slip rates range between 1-12 mm/yr, with a mean of 7 mm/yr and a mode of 8 mm/yr (dark gray in Figure 14B). The largest group of models (55%) predict slip rates between 8-12 mm/yr, and a smaller percentage (19%) of possible models predict fault slip rates ranging between 3-4 mm/yr.

After the initiation of faulting, the model allows for an acceleration in fault slip rate to occur between 0–14 Ma. The timing at which fault acceleration occurs is referred to as the "acceleration age" (Table 2). For the northern transect, possible acceleration ages range between 1–8 Ma, with a mean and mode of 6 Ma (light gray; Figure 14A). The majority of models (77%) show an acceleration age between 5–7 Ma, with the main peak centered at 6 Ma (Figure 14A).

After the acceleration age, the post-acceleration slip rate was allowed to vary between 0-12 mm/yr (Table 2). Possible post-acceleration slip rates range between 1-11 mm/yr with a mean of 3 mm/yr and a mode of 2 mm/yr (light gray; Figure 14B). The largest group of models (68%) predict post-acceleration rates between 1-2 mm/yr, and a few models (12%) predict a post-acceleration rate of 3 mm/yr.

The magnitude of slip along the GMD ranges between 30-75 km, with a mean between 45-50 km and a mode between 35-40 km (Figure 14C). The greatest number of fits are at 30-35

km (32%), with the rest of the data forming an asymmetrical bell curve, with the peak at 50-60 km.

Figure 13A shows a group of model runs that do not match the observed age trend (light gray lines). The plot also shows a second series of model runs that reproduced the observed sample ages well, with the exception of sample GM-12. Sample GM-12 has muscovite and biotite $^{40}Ar/^{39}Ar$ ages, but the Pecube modeling was unable to reproduce the muscovite age within 2-σ, and only ~1/3 of the best-fit models were able to reproduce the biotite age within 2-σ. If we model only the data that does not drastically over-estimate the biotite $^{40}Ar/^{39}Ar$ age for sample GM-15, these models reproduce the data with greater precision (dark gray, Figure 13A). Fault slip rates and initiation ages for these models show that overall trends do not change, and that the model results are more tightly constrained. These models require a fault initiation age between 12-11 Ma with acceleration at 6 Ma, an initial slip rate between 8-11 mm/yr, a post-acceleration rate of 1-2 mm/yr (Figure 14D, E), and an overall net slip between 60-70 km (Figure 14F).

4.3 Central Transect

The central transect corresponds to cross-section B-B' (Figure 7B), oriented parallel to slip-direction (280°), with the GMD striking ~010° with a 30° west dip (Figure11). A total of 12,000 models were possible. We employed the same filtering techniques described above, reducing the total number of possibilities to ~6,700 model runs. (See Table 2 for model parameters.) The initial results show that 56 of 6,700 models fit 8 out of 10 data points, no models were able to reproduces all 10 data points. Three samples were problematic: HUM02-71, HUM02-72, and HUM02-80 Both HUM02-71 and HUM02-72 were younger than the

surrounding samples, while HUM02-80 was significantly older (Figure 13B), although the ages were within 2-σ of the surrounding samples.

The fault initiation ages range between 18-9 Ma with a mean of 13 Ma and a mode of 11 Ma (dark gray; Figure 15A). A majority of the best-fit models (60%) predict an initiation age between 11–14 Ma (Figure 15A).

The initial-model slip rates range between 2–12 mm/yr, with a mean of 6 mm/yr and a mode of 4 mm/yr (dark gray; Figure 15B). The largest cluster of models (50%) predict an initial slip rate ranging between 3-5 mm/yr; when expanded between 2-7 mm/yr, the trend forms a Gaussian distribution that includes 78% of the models (Figure 15B).

The post-acceleration ages range between 1–13 Ma, with a mean of 7 Ma and a mode of 5 Ma (light gray; Figure 15A). There are two main peaks: the first between 6-3 Ma (34%) and the second between 9–13 Ma (41%).

The post-acceleration slip rate interval ranges between 1-10 mm/yr with a mean of 3 mm/yr and a mode of 3 mm/yr (light gray; Figure 15B). There is a group of data ranging between 1-3 mm/yr (93%) with the largest (62%) proportion of possible slip rates clustered at 3 mm/yr.

The model results for fault slip magnitude range between 35-75 km with a mean between 35-40 km and a mode between 40-41 km (Figure 15C). There is only one major distribution, where the majority (43%) of models predict between 35-55 km of fault slip.

The magnitude of the fault slip shows that the models do not constrain the parameters very well. This trend is also seen in the Modeled Age Plot (Figure 13B), but unlike the Cumulative Fault Slip Plot (Figure 13B), over half of the models produced a tight band (dark gray lines). Comparing the tightly grouped models, we see that the main difference is in their

ability to reproduce the easternmost (last) sample in the sampling transect. We chose to weight the models based on their ability to reproduce the last sample (dark gray lines), over models that were able to reproduce the second and fourth samples (light gray lines). This is because the last sample may represent a change in the thermal history or even entrance into the partial retention zone, whereas the 2nd and 4th samples deviated from their immediate surrounding samples, which renders their validity uncertain. When we remove all of the models that did not reproduce the last sample within 2-σ, the precision is increased. This results in a tighter constraint on the fault initiation age between 11–14 Ma, with an acceleration age between 11–13 Ma, an initial fault slip rate between 3-4 mm/yr, and a post-acceleration fault slip rate of 3 mm/yr (Figure 13D, E, and F). Within the resolution of the data, these results indicate that the fault slip rate remained constant at around ~3 mm/yr, with a fault slip magnitude between 35-50 km.

4.4 Southern Transect

The southern transect corresponds to cross-section C-C' (Figure 7C). Like the northern and central transects, the model is oriented in the general slip-direction (280°) with a planar fault striking ~010° and dipping 30° west (Figure 11). Unlike in the northern and central transects, the projected up-dip section of the fault does not roll over after breaking the surface. This is because early model testing showed a domed fault is not required to reproduce the general age trends.

Using these initial model parameters yields a total of 12,000 possible models. Using the filtering techniques described above, but increasing the possible total extension magnitude to 0-60 km, reduces the total number of possibilities to ~7,700. (See Table 2 for model parameters.) The range is decreased because field observations constraining fault slip estimates for this

portion of the fault are lower (24-32 km) [*Murphy and Copeland, 2005*]. The initial results show that 83 of 7,700 models fit 7 out of 8 data points, no models were able to reproduces all 8 data points. The two samples that the models did not reproduce well are HUM02-20 (48%) and HUM02-21 (52%) (Figure 13C).

Timing for fault initiation range between 7–15 Ma with a mean of 11 Ma and a mode of 8 Ma (dark gray; Figure 16A). The main peak of fault initiation is between 9-8 Ma (29%), with a second wider peak spanning between 15-11 Ma (48%).

The initial fault slip rate interval allowed by the model spans from 1-10 mm/yr, with a mean of 4 mm/yr and a mode of 2 mm/yr (dark gray; Figure 16B). The largest number of possible models (52%) requires an initial slip rate between 1-3 mm/yr, with a significant peak at 2 mm/yr.

For the southern transect, the timing of fault acceleration ranges between 9-1 Ma, with a mean of 4 Ma and a mode of 1 Ma (light gray; Figure 16A); 84% of the models requires an acceleration age ranging between 6-1 Ma, with three major peaks at 1 Ma, 3 Ma, and 6 Ma.

The post-acceleration rates range between 1-10 mm/yr, with a mean of 3 mm/yr and a mode of 2 mm/yr (light gray; Figure 16B). The main group (83%) range between 1-3 mm/yr with a significant peak at 2 mm/yr.

The predicted fault slip magnitude ranges between 15-70 km with a mean of 35-40 km and a mode of 20-25 km (Figure 16C). The largest group (59%) requires 20-35 km of fault slip. Further examination of Cumulative Fault Slip (Figure 13F) shows that the models do not constrain slip magnitude robustly because the range varies between 10-60 km. This is not the case with the Modeled Age Plot (Figure 13C), where the models are very tightly clustered, indicating a trade-off in precision between the two. Modeled Age (Figure 13C) suggests the

presence of two distinct "groups" of models. The first group is able to reproduce sample HUM02-20 (48%) while the second is able to reproduce sample HUM02-21 (52%) (Figure 13C). Examining the raw data (Table 1) for both data points reveals no clear reason to suspect that these zircon (U-Th)/He ages are questionable, so neither was excluded in our analysis. As with the northern and central transects, we examined each data set individually to reconcile the differences between the results of the two models.

A reexamination of Cumulative Fault Slip (Figure 13C) shows that almost all models could reproduce sample HUM02-20 (dark gray lines) with slip magnitude ranging between 20-35 km, while models reproducing sample HUM02-21 (light gray lines) predict a broader range of possible slip magnitudes (20-70 km). The models have the same results for the initiation age of faulting. This is also the case for the age of fault acceleration, with the exception of a large peak at 1 Ma for the HUM02-20 models (Figure 16D, F). This trend is not observed with the initial fault slip rate, where the HUM02-20 models show a rate of 1-2 mm/yr. While the set of HUM02-21 models do not present a major peak, they predict a significantly higher rate that is > 4 mm/yr. Both sets of models agree on a post-acceleration fault slip rate between 1-3 mm/yr. The main difference between the two sets of models lies in their initial fault slip rate. Because sample HUM02-20 is more definitive in its prediction of the initial fault slip rate, we give more weight to this set of models. Nonetheless, we note that we cannot exclude either model's predictions.

4.5 *Complications within the Pecube Results*

All three Pecube models (northern, central, and southern transects) were unable to reproduce all of the sample ages. We have identified at least three potential sources of error: (1) Errors within the thermochronologic ages. (2) Complications within the Pecube models

themselves. (3) An over simplification of the fault system and inherited assumptions in fault geometry. The first potential reason for this inaccuracy is within the thermochronologic data themselves. The model zircon (U-Th)/He thermochronometric age could differ from the "actual age" due to enrichment in parent isotopes of the zircon's rim. This enriched rim, possibly sourced from partial melts within the Himalaya, would result in the measured age being younger than the "actual age" [*Reiners, 2005*]. Thus, any samples measured from the intrusive leucogranites or grains with a complex growth history could produce ages that are incorrect.

The second source of error could result from the following complications within the Pecube modeling approach. (1) Because most of the samples were collected on or near the valley floor the smoothed DEM that we import into the model could have misplaced the "modeled" sample location 10's-100's of meters above the actual sample location. (2) The modeling also assumes all slip along the modeled fault is pure normal slip. (3) The geometry of the fault plane is assumed to be planar. These factors could result in the models inability to reproduce all of the sample ages.

The final source is the assumptions and over simplification of the fault system. The main assumption within this modeling is that all of the exhumation is driven by the GMD. But, other processes could influence the exhumation history of the footwall samples: (1) Isostatic rebound due to erosion of topography. (2) Corrugations within the footwall. (3) Exhumation related to slip along older shortening structures (e.g., the Great Counter Thrust and Main Central Thrust).

5. Discussion

5.1 Development of the Gurla Mandhata Detachment

The zircon (U-Th)/He data collected from the GMD footwall samples show that the footwall rocks cooled below 175-190°C by Late Miocene to Pliocene and are consistent with the entire footwall cooling rapidly. Possible ways to account for this age trend include the following: (1) allow for extremely fast exhumation of the footwall, and (2) compress the lower temperature isotherms towards the surface. It is likely that both of these processes occur during the structural development of the GMD. Based on the high U-Th concentration in the zircons processed (Table 1) in this study as well as the radiogenic heating measurements of Himalayan rocks [*Faccenda et al., 2008*], it is very likely that the crust below Gurla Mandhata has a higher-than-average geothermal gradient. When this factor is combined with the predicted slip rate for the GMD, we would expect "hot" footwall rocks to be exhumed to the surface at a fast enough rate to cause compression of the isotherms in the GMD footwall.

Our thermal modeling indicates fault initiation occurred between 11–14 Ma (Table 3), with a decrease in initiation age from north to south, and maximum net slip between 58-69 km (Figure 13, Table 3). Our estimates for initiation of faulting and maximum slip along the GMD system are consistent with previous work [*Murphy et al., 2002*]. The models predict initial slip rates from 8.0-11.0 mm/yr for the northern transect, and these rates decrease to 1-2 mm/yr ~6 Ma ago. In the central transect, the models predict a continuous slip rate between 3-4 mm/yr; in the southern transect, the models predict that the fault has a similar slip rate of 1-3 mm/yr. The initial rates for the northern and central transects bear similarity to the long-term slip rates reported by *Murphy et al.* [*2002*], while the mean slip rates and post-acceleration rates for all three transects are similar to the Quaternary slip rates reported by *Chevalier et al.,* [*2012*] (Table 4).

The modeling results from the Northern, Central, and southern transects are consistent with initiation of the GMD beginning in the north, followed by southward propagation of the

detachment system over time. This trend is evident upon examination of the best fit data (dark grey lines) in the Cumulative Extension plots (Figure 13), which reveal that net fault slip drops from 58-69 km in the north, to 17-35 km in the south. The highest mean slip rates of the three transects revealed in the northern transect is 5.0±0.9 mm/yr, and appears to decrease to 3.2±1.6 mm/yr for the southern transect. Collectively, these results suggest that the GMD initiated in the north and propagated southward.

5.2 Comparison with other Himalayan Extensional Structures

The modeled initiation age for the GMD is within ± 2 Ma of that estimated for the Ama Drime detachment system [*Jessup et al., 2008; Langille, et al., 2010*]. In addition, the Pliocene exhumation rate for the GMD is within ± 1 mm/yr of that estimated for Ama Drime [*Jessup et al., 2008; Langille et al., 2010*]. Both Ama Drime and the GMD have 10's of km of displacement associated with the main fault that result in the exhumation of mid-crustal Himalayan rocks [Murphy et al., 2002, Murphy and Copeland, 2005; Murphy, 2007; *Jessup et al., 2008; Langille, et al., 2010*]. Both extensional systems have similar ages obtained from biotite and muscovite $^{40}Ar/^{39}Ar$ data [*Murphy et al., 2002; Jessup et al., 2008*]. Although the GMD and Ama Drime extensional systems are significantly separated along the Himalayan arc, they share very similar histories and structural characteristics.

To the west of the GMD and across the Zada Basin is the Leo Pargil dome (Figure 1). $^{40}Ar/^{39}Ar$ muscovite and biotite ages from the footwall of the Leo Pargill dome range between 14.5±0.1-15.5±0.1 Ma, and apatite FT ages range between 1.7±0.3–9.9±0.8 Ma [*Thiede et al., 2006*]. The $^{40}Ar/^{39}Ar$ sample ages are much older than that observed for the GMD, and while the FT ages span a larger range, the results are consistent with the lower-temperature (U/Th)/He ages

obtained from the GMD footwall. This range in ages has been interpreted to represent a three-stage development beginning with rapid cooling between 16–14 Ma, followed by slow exhumation rates (0.07-0.16 mm/yr) between 10-4 Ma, and finally with rapid exhumation (0.4-1.9 mm/yr) from 4-0 Ma [*Thiede et al., 2006*]. Recent work has suggested that exhumation of the footwall could have started as early as 23 Ma [*Langille et al., 2012*]. These exhumation rates and younger timing relationships of the Leo Pargil dome are comparable to slower predicted fault slip rates from the Pecube modeling of the GMD. From these results, it seems that the GMD and the Leo Pargil dome have slightly different faulting histories, with the Leo Pargil fault initiating earlier and slipping at slower rates.

The modeled GMD slip rates are comparable to slower slip rate estimates for the Kung Co fault system. Thermochronologic data from the footwall of the Kung Co fault show zircon (U-Th)/He ages ranging between 8.3–12.9 Ma and Apatite (U-Th)/He ages ranging between 3.1–17.5 Ma [*Lee et al., 2011*]. The Kung Co fault initiated approximately 13 Ma ago, had a period of high fault slip rates (> 7 mm/yr) between 13–10 Ma, and then slowed from 9-0 Ma [*Lee et al., 2011*]. Both fault systems yield similar ages for faulting initiation, but only the lowest rates modeled on the Kung Co fault are comparable to the modeling results for the GMD system.

5.4 Comparison of GMD to KF

For our purposes, the slip-rate data from the southern portion of the KF are more relevant. Slip rates inferred from geodesy for the central KF have mixed results with lower bounds ranging between 1-6 mm/yr [*Chen et al., 2004; Wright et al., 2004; Loveless and Meade, 2011; Wang and Wright, 2012*], to upper bounds between 5-15 mm/yr [*Banerjee and Burgmann, 2002; Jade et al., 2004; Zhang et al., 2004*]. Fault slip rate estimates based on ^{10}Be cosmogenic nuclide

dating of boulders from offset geomorphic landforms have also produced both low [*Brown et al., 2002*] and high fault slip rates [*Chevalier et al., 2005a, 2005b, 2011, 2012*], which are strongly dependant on the preferred offset reconstructions and sampling strategy [e.g. Brown et al., 2005]. The long-term geologic slip rates for the southern KF range between 4.7-9 mm/yr [*Murphy et al., 2000; Wang et al., 2009; Wang et al., 2012*]; for the central KF, these values range between 7-15 mm/yr [*Searle et al., 1998; Lacassin et al., 2004; Valli et al., 2007, 2008; Wang et al., 2011*].

The mean modeled slip rates in this study match slip rate estimates for the KF across different timescales (Figure 17). Some of the best rate agreements are with the geodedic rates [*Chen et al., 2004; Wright et al., 2004; Zhang et al., 2004; Jade et al., 2004, 2010; Loveless and Meade, 2011*] and the slower, long-term slip rates [*Murphy et al., 2000; Phillips et al., 2004; Rutter et al., 2007; Wang et al., 2012*], while only a single rate based on cosmogenic nuclides is in agreement with our mean modeled rate (Figure 17) [*Brown et al., 2002*]. The individual transect results show that the fault slip rates obtained for the northern transect match with all of the KF slip rate data, but this is mostly due to the very high initial fault slip rate. Both the central and southern transects have slower fault slip rates (< 5 mm/yr) that are in agreement with shorter timescales obtained with geodesy (Figure 17).

From these results, there is compelling evidence that the GMD (11–14 Ma) and the southern portion of the KF [~13 Ma; *Murphy et al., 2000*] have similar ages of fault initiation and magnitudes of fault slip. In addition, the fault slip rates modeled for the GMD are comparable to the slip rate data for the central and southern KF across several timescales (10-10^6 years) (Figure 17). These results suggest that the GMD has been kinematically linked to the KF since 14-11 Ma, and that the GMD transfers slip southeastward into the Humla fault and High Himalaya (Figure 5).

5.5 Implications for Tectonic Models

To thoroughly evaluate the viability of the tectonic models described in section 1.1 we compare the results from this study to the predictions made by each of the four models beginning with lateral extrusion, oroclinal bending, radial spreading, and finally oblique convergence.

5.5.1 Lateral Extrusion

The lateral extrusion model predicts high rates (>1 cm/yr) and magnitudes (100's of km) of dextral slip on both the KF and IYS zone. The model also describes that most of the dextral motion associated with the KF is transferred into the IYS zone. The results of this study show that the GMD accommodates the entire dextral shear associated with the southern KF, which implies that negligible strain is transferred along the IYS past the GMD since the mid Miocene. Additionally, there is strong doubt that the IYS is an active dextral structure based on the lack of any compelling evidence for active faulting along the IYS east of longitude 82.3° (Figure 18B), and clear cross-cutting field relationships documented at the southern end of the Lopukangri rift, where the IYS zone and Great Counter thrust are cut and offset by the N-striking Lopukangri normal fault [*Murphy et al., 2010*].

5.5.2 Oroclinal Bending

Comparing our results with those predicted by the oroclinal bending model, we see that our results do not match its predictions. This model predicts that extension rates should increase towards the frontal portions of the thrust belt. However, when our data is combined with

geodetic data for western Nepal [*Larson et al., 1999; Jouanne et al., 2004*], there is an apparent decrease in dextral shear towards the Himalayan front. Also, the predicted kinematics for the KF, faults in central Tibet, and southeastern Tibet do not match field observations. In particular, model predictions require sinistral motion on the KF, which are opposite to field observations of dextral faulting [*Ratschbacher et al., 1994; Searle et al., 1998; Murphy et al., 2000*].

5.5.3 Radial Spreading

There is strong agreement between our results and prediction made by the radial spreading model. This model predicts that the magnitude of slip decreases towards the Himalayan front. Our results when combined with data for the KF and geodetic data from western Nepal [*Larson et al., 1999; Jouanne et al., 2004*] show a decrease in arc-parallel slip magnitude and rate towards the Himalayan front. However, geodetic data for the Himalaya show an increase in the arc-parallel component west of the central Himalaya [*Gan et al., 2007; Styron et al., 2011*]. This is inconsistent with predictions in the radial spreading model, which requires a constant arc-parallel velocity across the entirety of the Himalayan front. From the GPS data, it is apparent that although our study agrees with the predictions of the radial spreading model, the geodetic observations imply that the radial spreading model is likely not operating today.

5.5.4 Oblique Convergence

There is strong agreement between our study and the predictions made by the oblique convergence model. In particular,his model predicts that the magnitude of extension and strike-slip faulting increases westward along the Himalaya and appears to be controlled by the

increasing convergence obliquity between India and the Himalaya. Our data in combination with other field-based studies are consistent with this prediction [*Searle et al., 1998; Larson et al., 1999; Murphy et al., 2000, 2002; Jouanne et al., 2004; Robinson et al., 2009*]. Additionally, oblique convergence predicts an increase in the arc-parallel component of displacement west of the central Himalaya. Recent GPS compilations and analysis [*Gan et al., 2007, Styron et al., 2011*] indicate an increase is the arc-parallel component of the surface displacement field west of the central Himalaya. Finally, our study indicates that the GMD and KF systems are acting together as a kinematically coordinated fault system, which is also consistent with oblique convergence.

6. Conclusions

Our study in southwest Tibet along the GMD can be best summarized by the following points:

1. (U-Th)/He dating of zircon from 21 samples collected along three transects yields Late Neogene ages, consistent with rapid exhumation of the GMD footwall. The sample transects were evaluated using the Pecube finite element software, which was used to run 7,700-6,700 models per transect to constrain the initiation and slip history for the GMD. Our results are consistent with a southward propagating history, with the highest net slip (50-60 km) in the north that decreases to less than half that at its southernmost segment (15-30 km). Modeling results for fault slip rates for the central and southern segments are similar with slower fault slip rates (~1-4 mm/yr), while the northern segment experiences higher rates of faulting (5.0±0.9 mm/yr).

2. Gurla Mandhata is one of several examples for demonstrating how arc parallel extension is accommodated in the High Himalaya. Examples of other extensional structures along the High Himalaya near the Tibetan border include the Leo Pargil and Ama Drime domes, and the Kung Co rift, all of which initiated in the early Neogene. While the above mentioned structures do not have a direct linkage with the Karakoram fault system, this and previous studies demonstrate that the structural and kinematic history of the GMD fault system is comparable to the other Himalayan extensional structures thus highlighting the importance of active extension within the Himalayan thrust wedge.

3. The kinematic relationships obtained from Pecube modeling results indicate that the GMD system had a similar initiation age and slip rate compared with the Karakoram fault, consistent with the GMD acting as a right-step extensional feature within a southward propagating system of dextral shear. If this relationship between the GMD and Karakoram fault is correct, this structural relationship requires that fault slip bypasses the IYS zone and transfers slip into the High Himalaya. Furthermore, this model is most consistent with active faults in southwest Tibet and western Nepal acting in the context of oblique convergence.

References:

Armijo, R., P. Tapponnier, J. L. Mercier, H. Tong-Lin (1986), Quaternary extension in southern Tibet: Field observations and tectonic implications, Journal of Geophysical Research, 91, 13803-13872.

Armijo, R., P. Tapponnier, H. Tonglin (1989), Late Cenozoic Right-Lateral Strike-Slip Faulting in Southern Tibet, Journal of Geophysical Research, 94, 2787-2838.

Banerjee, P., R. Burgmann (2002), Convergence across the northwest Himalaya from GPS measurements, Geophysical Research Letters, 29, 1-4.

Beaumont, C., R. A. Jamieson, M. H. Nguyen, S. Medvedev (2004), Crustal channel flows: 1. Numerical models with applications to the tectonics of the Himalayan-Tibetan orogen, Journal of Geophysical Research, 109, B06406.

Besse, J., V. Courtillot, J. P. Pozzi, M. Westphal, Y. X. Zhou (1984), Palaeomagnetic estimates of crustal shortening in the Himalayan thrusts and Zangbo suture, Nature, 311, 621-626.

Bird, P., (1991), Lateral extrusion of lower crust from under high topography, in the isostatic limit, Journal of Geophysical Research, 96, 10,275–10,286.

Brandon, M. T., M. K. Roden-Tice, J. I. Garver, (1998), Late Cenozoic exhumation of the Cascadia accretionary wedge in the Olympic Mountain, northwest Washington State, Geological Society of America Bulletin, 110, 985-1009

Braun, L., (2003), Pecube: a new finite-element code to solve the 3D heat transport equation including the effects of a time-varying, finite amplitude surface topography, Computers & Geosciences, 29, 787-794.

Brookfield, M. E., (1993), The Himalayan passive margin from Precambrian to Cretaceous times, Sedimentary Geology, 84, 1-35.

Brown, E. T. (2005), Comment on "Slip-Rate Measurements on the Karakorum Fault May Imply Secular Variations in Fault Motion", Science, 309, 1326, DOI: 10.1126/science.1112508.

Brown, E.T., R. Bendick, D. L. Bourles, V. Gaur, P. Molnar, G. M. Raisbeck, F. Yiou (2002), Slip rates of the Karakorum fault, Ladakh, India, determined using cosmic ray exposure dating of debris flows and moraines, Journal of Geophysical Research, 107, 1-19.

Burchfield, B. C., C. Zhiliang, K. V. Hodges, L. Yuping, L. H. Royden, D. Changrong, X. Jiene (1992), The South Tibetan detachment system, Himalayan orogen's contemporaneous with the parallel to shortening in a collisional mountain belt, Geological Society of America, Special Publication, 269, 1-15.

Burg, J. P., G. M. Chen, (1984), Tectonics and structural zonation of southern Tibet, Nature, 311, 219-223.

Chen, Q., J. T. Freymueller, Z. Yang, C. Xu, W. Jiang, Q. Wang, J. Liu (2004), Spatially variable extension in southern Tibet based on GPS measurements, Journal of Geophysical Research, 109, 1-60.

Chen, W.P., M., Martin, T.L., Tseng, R. L. Nowack, S.H., Hung, B.S., Huang (2010), Shear-wave birefringence and current configuration of converging lithosphere under Tibet, Earth and Planetary Science Letters. 295, 297-304.

Chevalier, M. L., F. J. Ryerson, P. Tapponnier, R. C. Finkel, J. Van Der Woerd, L. Haibing, L. Qing (2005a), Slip rate measurements on the Karakorum fault may imply secular variations in fault motion, Science, 307, 411–414.

Chevalier, M.-L., F. J. Ryerson, P. Tapponnier, R. C. Finkel, J. Van Der Woerd, L. Haibing, L. Qing (2005b), Response to comment on "Slip rate measurements on the Karakorum fault may imply secular variations in fault motion", Science, 309, 1326, DOI:

10.1126/science.1112629.

Chevalier, M.-L., H. Li, J. Pan, J. Pei, F. Wu, W. Xu, Z. Sun, D. Liu, (2011), Fast slip rate along the northern end of the Karakorum fault system, western Tibet, Geophysical Research Letters, 38, 1-7.

Chevalier, M. L., P. Tapponnier, J. V. Woerd, F. Ryerson, R. C. Finkel, H. Li (2012), Spatially constant slip rate along the southern segment of the Karakorum fault since 200 ka, Tectonophysics, 530-531, 152-179.

Copley, A., (2008), Kinematics, and dynamics of the southeastern margin of the Tibetan Plateau, Geophysics Journal International, 174, 1081-1100.

Copley, A., and D. McKenzie (2007), Models of crustal flow in the India-Asia collision zone, Geophysical Journal International, 169, 683–698.

DeCelles, P. G., G. E. Gehrels, J. Quade, T. P. Ojha (1998), Eocene-early Miocene foreland basin development and the history of Himalayan thrusting, western and central Nepal, Tectonics, 17, 741-765.

DeCelles, P. G., G. E. Gehrels, J. Quade, B. LaReau, M. Spurlin (2000), Tectonic implications of U-Pb zircon ages of the Himalayan orogenic belt in Nepal, Science, 288, 497-499.

Dewane, T. J., D. F. Stockli, C. Hager, M. Taylor, L. Ding, S. Wallis (2006), Timing of Cenozoic E-W Extension in the Tangra Yum Co-Kung Co Rift, south-central Tibet, American Geophysical Uninion, Fall Meeting, abstract # T34C-04.

England, P.C., and G. A. Houseman (1988), The mechanics of the Tibetan Plateau, Royal Society of London Philosophical Transactions, ser. A, 326, 301–319.

Faccenda, M., T. V. Gerya, S. Shakraborty (2008), Styles of post-subduction collisional orogeny: Influence of convergence velocity, crustal rheology and radiogenic heat production,

Lithos, 103, 257-287.

Gaetani, M., E. Garzanti (1991), Multicyclic History of the Northern India Continental Margin [Northwestern Himalaya], American Association of Petroleum Geologist Bulliten, 75, 1427-1446.

Gan, W., P. Zhang, Z. Shen, Z. Niu, M. Wang, Y. Wan, D. Zhou, J. Cheng (2007), Present-day crustal motion within the Tibetan Plateau inferred from GPS measurements, Journal of Geophysical Research, 112, 1-14.

Harrison, T. M., P. Copeland, W. S. F. Kidd, O. M. Lovera (1995), Activation of the Nyainqentanghla Shear Zone: Implications for uplift of the southern Tibetan Plateau, Tectonics, 14, 658-676.

Heim, A., A. Gansser (1939), Central Himalaya, geological observations of the Swiss expeditions 1936, Memoire Societe Helvetique Science, Naturelle, 73, 1-245.

Hodges, K. V., (2000), Tectonics of the Himalaya and southern Tibet from two perspectives, Geologic Society of America Bulletin, 112, 324-350.

Jade, S., B. C. Bhatt, Z. Yang, R. Bendick, V. K. Gaur, P. Molnar, B. M. Anand, D. Kumar (2004), GPS measurements from the Ladakh Himalaya, India: Preliminary test of plate-like or continuous deformation in Tibet, Geological Society of America Bulletin, 116, 1385-1391.

Jade, S., R. H. J. Raghavendra Rao, M. S. M. Vijayan, V. K. Gaur, B. C. Bhatt, K. Kumar, S. Jaganathan, M. B. Ananda, P. Dileep Kumar (2010), GPS-derived deformation rates in northwestern Himalaya and Ladakh, International Journal of Earth Sciences, 100, 1293-1301, doi:10.1007/s00531-010-0532-3.

Jessup, M. J., D. L. Newell, J. M. Cottle, A. L. Berger, J. A. Spotila (2007), Orogenparallel

extension and exhumation enhanced by denudation in the trans-Himalayan Arun River gorge, Ama Drime Massif, Tibet-Nepal, Geology, 36, 587-590.

Jessup, M. J., D. L. Newell, J. M. Cottle, A. L. Berger, J. A. Spotila (2008), Orogen-parallel extension and exhumation enhanced by denudation in the trans-Himalayan Arun River gorge, Ama Drime Massif, Tibet-Nepal, Geology, 36, 587-590.

Jouanne, F., J. L. Mignier, J. F. Gamond, P. Le Fort, M. R. Pandey, L. Bollinger, M. Flouzat, J. P. Avouac (2004), Current Shortening across the Himalayas of Nepal, Geophysical Journal International, 157, 1-14.

Kapp, J., T. M. Harrison, P. Kapp, M. Grive, O. M. Lovera, D. Lin (2005), Nyainqentanglha Shan: A window into the tectonics, thermal, and geochemical evolution of the Lhasa block, southern Tibet, Journal of Geophysical Research, 110, 1-23.

Kapp, P., M. Taylor, D. Stockli, L. Ding (2008), Development of active low-angle normal fault system during orogenic collapse: Insight form Tibet, Geology, 36, 7-10.

Klootwijk, C.T., P. J. Conaghan, and C. M. Powell (1985), The Himalayan Arc—Large-scale continental subduction, oroclinal bending and back-arc spreading, Earth and Planetary Science Letters, 75, 167–183.

Lacassin, R., F. Valli, N. Arnaud, P. H. Leloup, J. L. Paquette, L. Haibing, P. Tapponnier, M. L. Chevalier, S. Guillot, G. Maheo, X. Zhiqin (2004), Large-scale geometry, offset and kinematic evolution of the Karakorum fault, Tibet, Earth and Planetary Science Letters, 219, 255-269.

La Langille, J. M., M. J. Jessup, J, M. Cottle, D. Newell, G. Seward (2010), Kinematic evolution of the Ama Drime detachment: Insights into orogen-parallel extension and exhumation of the Ama Drime Massif, Tibet-Nepal, Journal of Structural Geology, 32, 900-919,

doi:10.1016/j.jsg.2010.04.005.

Langille, J. M., M. J. Jessup, J, M. Cottle, G. Lederer, T. Ahmad (2012), Timing of metamorphism, melting and exhumation of the Leo Pargil dome, northwest India, Journal of Metamorphic Geology, 30, 769-791, doi:10.1111/j.1525-1314.2012.00998

Larson, K., R., Burgmann, R. Bilham, J. Freymuller (1999), Kinematics of the India-Eurasia collision Zone from GPS measurements, Journal of Geophysical Research, 104, 1077-1093.

Lee, J., C. Hager, S. R. Wallis, D. F. Stockli, M. J. Whitehouse, M. Aoya, Y. Wang (2011), Middle to late Miocene extremely rapid exhumation and thermal reequilibration in the Kungo Co rift, southern Tibet, Tectonics, 30, TC2007, doi:10.1029/2010TC002745.

Li, D., and A. Yin (2008), Orogen-parallel, active left-slip faults in the Eastern Himalaya: Implications for the growth mechanism of the Himalayan Arc, Earth and Planetary Science Letters, 274, 258–267.

Loveless, J.P., and B. J. Meade (2011). Partitioning of localized and diffuse deformation in the Tibetan Plateau from joint inversions of geologic and geodetic observations. Earth and Planetary Science Letters, 303, 11–24.

Mercier, J., R. Armijo, P. Tapponnier, E. Carey-Gailhardis, H. Lin (1987), Change from late Tertiary compression to Quaternary extension in southern Tibet during the India-Asia collision, Tectonics, 6, 275-304.

McCaffrey, R., and J. Nabelek (1998), Role of oblique convergence in the active deformation of the Himalayas and southern Tibet plateau, Geology, 26, 691-694.

Miller, C., R. Schuster, U. Klötzli, W. Frank, F. Purtscheller (1999), Post-Collisional Potassic and Ultrapotassic Magmatism in SW Tibet: Geochemical and Sr-Nd-Pb-O Isotopic

Constraints for Mantle Source Characteristics and Petrogenesis, Journal of Petrology, 40, 1399-1424.

Murphy, M A., (2007), Isotopic characteristics of the Gurla Mandhata metamorphic core complex: Implications for the architecture of the Himalayan orogen. Geology, 35, 983-986.

Murphy, M. A., and A. Yin (2003), Structural evolution and sequence of thrusting in the Tethyan fold-thrust belt and Indus-Yalu suture zone, southwest Tibet, Geological Society of America Bulletin, 115, 21-34.

Murphy, M. A., and P. Copeland (2005), Transtensional deformation in the central Himalaya and its role in accommodating growth of the Himalayan orogen, Tectonics, 24, 119.

Murphy, M. A., and P. W. Burgess (2006), Geometry, kinematics, and landscape characteristics of an active transtension zone, Karakoram fault system, Southwest Tibet, Journal of Structural Geology, 28, 263-283.

Murphy, M. A., A. Yin, P. Kapp, T. M. Harrison, D. Ling, G. Jinghui (2000), Southward propagation of the Karakoram fault system, southwest Tibet: timing and magnitude of slip, Geology, 28, 451–454.

Murphy, M. A., A. Yin, P. Kapp, T. M. Harrison, C. E. Manning, F. J. Ryerson, D. Lin, G. Jinghui (2002). Structural evolution of the Gurla Mandhata detachment system, southwest Tibet: implications for the eastward extent of the Karakoram fault system, Geological Society of America Bulletin, 114, 428–447.

Murphy, M. A., J. E. Saylor, L. Ding (2009), Late Miocene topographic inversion in southwest Tibet based on integrated paleoelevation reconstructions and structural history, Earth and Planetary Science Letters, 282, 1-9.

Murphy, M. A., V. Sanchez, M. H. Taylor (2010), Syncollisional extension along the Indian-Asian suture zone, south-central Tibet: Implications for crustal deformation of Tibet, Earth and Planetary Science Letters, 290, 233-243.

Nabelek, J., G. Hetenyi, J. Vergne, S. Sapkota, B. Kafle, M. Jiang, H. Su, J. Chen, B. S. Huang (2009), Underplating in the Himalaya-Tibet Collision Zone Revealed by the Hi-CLIMB Experiment, Science, 325, 1371-1374.

Nabelek, P. I., A. G. Whittington, A. M. Hofmeister (2010), Strain heating as a mechanism for partial melting and ultraheigh temperature metamorphism in convergent orogens: Implications of temperature-dependent thermal diffusivity and rheology, Journal of Geophysical Research, 115, B12417, doi:10.1029/2010JB007727.

Nabelek, P. I., J. L. Nabelek (2011) A strain-heating model for the seismic low-velocity zone alont the Main Himalaya Thrust, Journal of Himalayan Earth Sciences, 44, 62-63.

Pan, Y., W. S. F. Kidd (1992), Nyainqentanglha shear zone: A late Miocene extensional detachment in the southern Tibetan Plateau, Geology, 20, 775-778.

Parrish, R. R., and K. V. Hodges (1996), Isotopic constraints on the age and provenance of the Lesser and Greater Himalayan sequences, Nepalese Himalaya, Geological Society of America Bulletin, 108, 904-911.

Phillips, R. J., R. R. Parrish, M. P. Searle (2004), Age constraints on ductile deformation and long-term slip rates along the Karakoram fault zone, Ladakh, Earth and Planetary Science Letters, 226, 305-319.

Pullen A., P. Kapp, P. G. DeCelles, G. E. Gehrels, L. Ding (2011),Cenozoic anatexis and exhumation of Tethyan Sequence rocks in the Xiao Gurla Range, Southwest Tibet, Tectonophysics, 501, 28-40.

Ratschbacher, L., W. Frisch, G. Liu, C. Chen (1994), Distributed deformation in southern and western Tibet during and after the India-Asia collision, Journal of Geophysical Research, 99, 19,917– 19,945.

Reiners, P.W., (2005), Zircon (U-Th)/He Thermochronometry, Thermochronology, Reviews in Mineralogy and Geochemistry, 58, 151-176.

Reiners, P. W., K. A. Farley, H. J. Hickes (2002), He diffusion and (U-Th)/He thermochronometry of zircon: initial results from Fish Canyon Tuff and Gold Butte, Tectonophysics, 349, 297-308.

Robinson, A. C., (2009), Geologic offsets across the northern Karakorum fault: Implications for its role and terrane correlations in the western Himalayan-Tibetan orogen, Earth and Planetary Science Letters, 279, 123-130.

Robinson, A. C., A. Yin, O. M. Lovera (2010), The role of footwall deformation and denudation in controlling cooling age patterns of detachment systems: An application to the Kongur Shan extensional system in the Eastern Pamir, China, Tectonophysics, 496, 28-43.

Rowley, D. B., (1996), Age of collision between India and Asia: A review of the stratigraphic data: Earth and Planetary Science Letters, 145, 1-13.

Rutter, E. H., D. R. Faulkner, K. H. Brodie, R. J. Phillips, M. P. Searle (2007), Rock deformation processes in the Karakoram fault zone, Eastern Karakoram, Ladakh, NW India, Journal of Structural Geology, 29, 1315-1326.

Sanchez, V., M. A. Murphy, W. R. Dupre, L. Ding, R. Zhang (2010), Structural evolution of the Neogene Gar Basin, western Tibet: implications for releasing bend development and drainage patters, Geological Society of America Bulletin, 122, 926-945.

Sanchez, V. I., M. A. Murphy, A. C. Robinson, T. J. Lapen, M. T. Heizler (2012), Tectonic evolution of the Indian-Asia suture zone since Middle Eocene time, Lopukangri area, south-central Tibet, Journal of Asian Earth Sciences, in press.

Schill, E., E. Appel, O. Zeh, V. Singh, P. Gautam (2001), Coupling of late-orogenic tectonics and secondary pyrrhotite remanences: Towards a separation of different rotation processes and quantification of rotational underthrusting in the western Himalaya [northern India], Tectonophysics, 337, 1–21.

Schill, E., C. Crouzet, P. Gautam, V. K. Singh, E. Appel (2002), Where did rotational shortening occur in the Himalayas? Inferences from palaeomagnetic remagnetisations, Earth and Planetary Science Letters, 203, 45–57.

Schill, E., E. Appel, C. Crouzet, P. Gautam, F. Wehland, M. Staiger (2004), Oroclinal bending versus regional significant clockwise rotations in the Himalayan arc-Constaints from secondary purrhotite remanences, Geological Society of America Special Paper, 383, 3-85.

Searle, M. P., (1986), Structural evolution and sequence of thrusting in the High Himalayan, Tibetan—Tethys and Indus suture zones of Zanskar and Ladakh, Western Himalaya, Journal of Structural Geology, 8, 923-936.

Searle, M.P., R. F. Weinberg, W. J. Dunlap (1998), Transpressional tectonics along the Karakoram fault zone, northern Ladakh: Constraints on Tibetan extrusion, *in* Holdsworth, R.E., et al., eds., Continental transpressional and transtensional tectonics, Geological Society of London Special Publication 135, 307– 326.

Seeber, L., and A. Pecher (1998), Strain partitioning along the Himalayan arc and the Nanga Parbat antiform, Geology, 26, 791-794.

Stockli, D.F., (2005), Application of low-temperature thermochronometry to extensional tectonic settings, Reviews in Mineral Geochemistry, 58, 411-448.

Styron, R., M. Taylor, K. Okoronkwo (2010), Database of active structures from the Indo-Asian Collision, Eos (Transactions, American Geophysical Union), 91, no. 20.

Styron, R. H., M. H. Taylor, M. A. Murphy (2011), Oblique convergence, arc-parallel extension, and the role of strike-slip faulting in the High Himalaya, Geosphere, 7, 582-596.

Styron, R. H., M. H., Taylor, K. E., Sundell, D. F., Stockli, J. A. G. Oalmann, A. T., McCallister, D. Liu, A. Moller, L. Ding, (in review), Miocene initiation and acceleration of extension in the South Lunggar rift, western Tibet: evolution of an active detachment system from structural mapping and (U-Th)/He thermochronology, Tectonics, in review.

Tagami, T., K. A. Farley, D. F. Stockli (2003), (U-Th)/He geochronology of zircon using Nd-YAG laser heating, Earth and Planetary Science Letters, 207, 57-67.

Tapponnier, P., J. L. Mercier, R. Armijo, H. Tonglin, Z. Ji (1981), Field evidence for active normal faulting in Tibet, Nature, 294, 410-414.

Tapponnier, P., G. Peltzer, A. Y. Le Dain, R. Armijo, P. Cobbold (1982), Propagating extrusion tectonics in Asia: New insights from simple experiments with plasticine, Geology, 10, 611 –616.

Tapponnier, P., Z. Q. Xu, F. Roger, B. Meyer, N. Arnaud, G. Wittlinger, J. S. Yang (2001), Oblique stepwise rise and growth of the Tibet Plateau, Science, 294, 1671-1677.

Taylor, M., and A. Yin (2009), Active structures of the Himalayan-Tibetan orogen and their relationships to earthquake distribution, contemporary strain field, and Cenozoic volcanism, Geophere, 5, 199-214.

Taylor, M., A. Yin, F. J. Ryerson, P. Kapp, L. Ding (2003), Conjugate strike-slip faulting along

the Bangong-Nujiang suture zone accommodates coeval east-west extension and north-south shortening in the interior of the Tibetan Plateau, Tectonics, 22, 1-25.

Taylor, M., and G. Peltzer (2006), Current slip rates on conjugate strike-slip faults in central Tibet using synthetic aperture radar interferometry, Journal of Geophysical Research, 111, B12402, doi:10.1029/2005JB004014.

Thiede, R., J. Arrowsmith, B. Bookhagen, M. McWilliams, E. Sobel, M. Strecker (2006). Dome formation and extension in the Tethyan Himalaya, Leo Pargil, northwest India, Geological Society of America Bulletin, 118, 635-650.

Valli, F., N. Arnaud, P. H. Leloup, E. R. Sobel, G. Maheo, R. Lacassin, S. Guillot, H. Li, P. Tapponnier, Z. Xu (2007), Twenty million years of continuous deformation along the Karakorum fault, western Tibet: a thermochronological analysis, Tectonics, 26, 1-26.

Valli, F., J. L. Leloup, N. Arnaud, H. Li, P. Tapponnier, R. Lacassin, S. Guillot, D. Liu, E. Deloule, Z. Xu, G. Maheo (2008), New U-Th/He constraints on timing of shearing and long-term slip rate on the Karakorum fault, Tectonics, 27, 1-33.

Wang, S., E. Wang, X. Fang, Q. Lai (2011), U-Pb SHRIMP and $^{40}Ar/^{39}Ar$ ages constrain the deformation history of the Karakoram fault zone [KFZ], SW Tibet, Tectonophysics, 509, 208-217.

Wang, S., C. Wang, R. J. Phillips, M. A. Murphy, X. Fang, Y. Yue (2012), Displacement along the Karakoram fault, NW Himalaya, estimated from LA-ICP-MS U-PB dating of offset geologic markers, Earth and Planetary Science Letter, 337-338, 156-163.

Wang, S., and T. J. Wright (2012), Satellite geodetic imaging reveals internal deformation of western Tibet, Geophysical Research Letters, 39, L07303, doi:10.1029/2012GL051222.

Wang, S., X. Fang, Q. Lai, D. Zheng, Y. Wang (2009), New radiometric dating constrains the time for initiation of the Karakorum fault zone [KFZ], SW Tibet, Tectonophysics, 475, 503-513.

Wolf, M. R., and D. F. Stockli (2010), Zircon (U-Th)/He thermochronometry in the KTB drill hole, Germany, and its implications for bulk He diffusion kinetics in zircon, Earth and Planetary Science Letter, 295, 69-82.

Wright, T.J., B. Parsons, P. C. England, E, J, Fielding (2004), InSAR observations of low slip rates on the major faults of western Tibet, Science, 305, 236–239.

Yin, A., and M. Harrison (2000), Geologic evolution of the Himalayan-Tibetan orogen, Earth Planet Science, 28, 211-280.

Yin, A., P. A. Kapp, M. A. Murphy, C. E. Manning, T. M. Harrison, M. Grove, D. Lin, D. Xi-Guang, W. Cun-Ming (1999), Significant late Negoene east-west extension in northern Tibet, Geology, 27, 787-790.

Zhang, P.Z., Z. Shen, M. Wang, W. J. Gan, R. Burgmann, P. Molnar (2004), Continuous deformation of the Tibetan Plateau from global positioning system data, Geology, 32, 809–812.

Zhu, B., W. S. F. Kidd, D. B. Rowley, B. S. Currie, N. Shafique (2005), Age of Initiation of the India-Asia Collision in the East-Central Himalaya, The Journal of Geology, 2005, 113, 265-285.

Figures:

Figure 1:

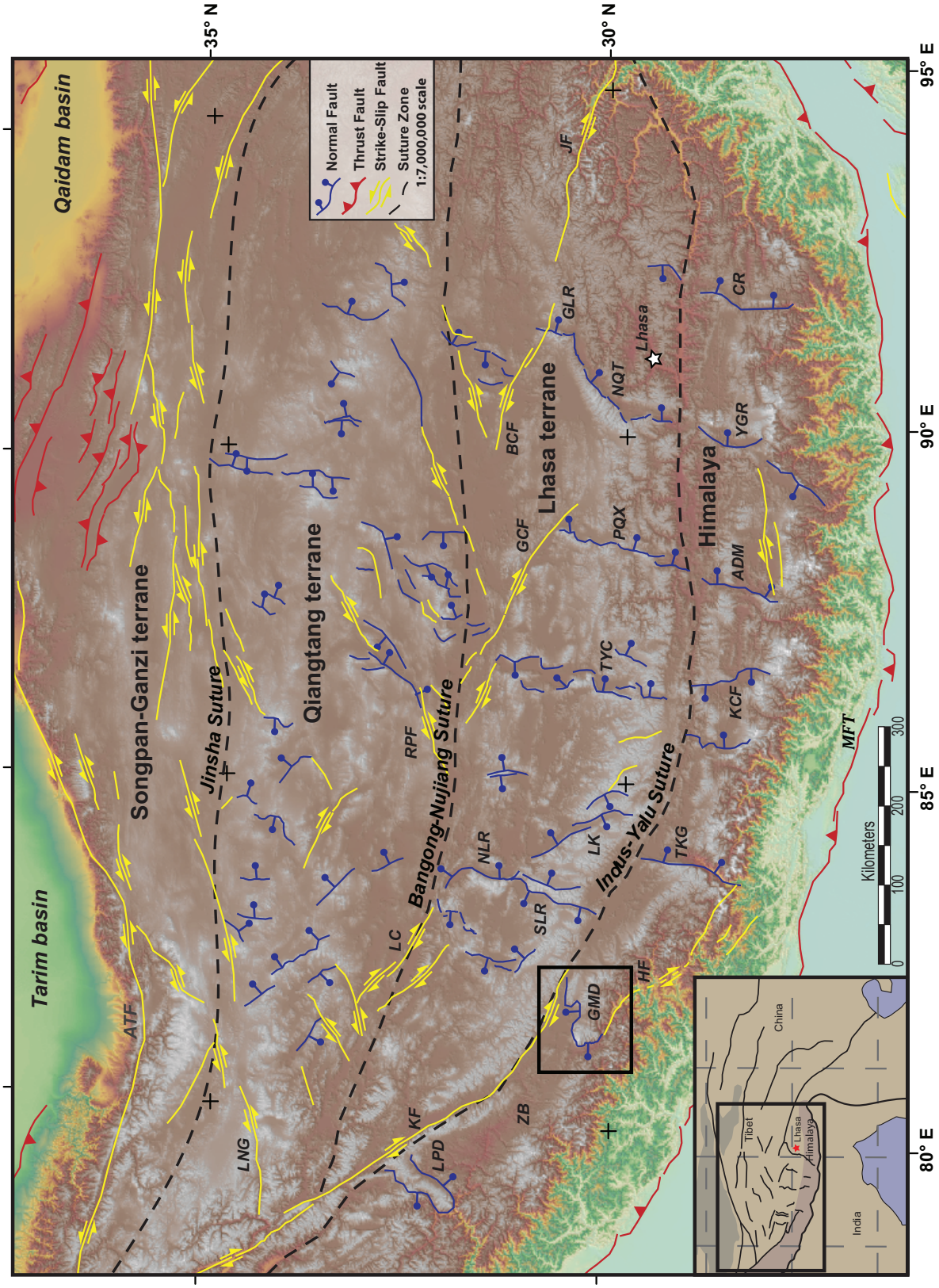
Qaidam basin
Tarim basin
Songpan-Ganzi terrane
Qiangtang terrane
Lhasa terrane
Himalaya
Jinsha Suture
Bangong-Nujiang Suture
Indus-Yalu Suture
MFT
Lhasa
Normal Fault
Thrust Fault
Strike-Slip Fault
Suture Zone
1:7,000,000 scale
ATF
LNG
KF
LPD
ZB
LC
RPF
NLR
SLR
LK
GMD
HF
TKG
KCF
TYC
PQX
GCF
BCF
GLR
NQT
JF
ADM
YGR
CR
Kilometers
0
100
200
300
80° E
85° E
90° E
95° E
35° N
30° N
China
Tibet
Lhasa
Himalaya
India

Figure 1:

Shaded relief map of the Tibetan plateau showing the distribution of active faults. Thrust faults are red, normal faults are blue, and strike-slip faults are yellow. The black square shows the area covered by the geologic map (Figure 6). The dashed black lines represent suture zones. ADM - Ama Drima Massif; ATF – Altyn Tagh fault; BCF – Beng Co fault; CR – Coma Rift; GCF - Gyaring Co fault; GLR – Gulu Rift; GMD – Gurla Mandhata Detachment; HF – Humla fault; JF – Jiali fault; KCF – Kung Co fault; KF – Karakoram fault; KUF – Kunlun fault; LC – Lamu Co fault; LK – Lopukangri; LPD - Leo Pargil Dome; LNG – Longmu Co-Gozha Co fault; MFT – Main Frontal Thrust; NLD – North Lungar Detachment; NQT – Nyainqentanglha Shan; PQX – Pumqu-Xianza Rift; RPF – Rigangpei Co fault; SLR – South Lunggar Detachment: TKG – Thakkola Graben; TYC – Tangra Yum Co Rift; YGR – Yadong Gulu Rift; ZB – Zada Basin. Modified after *Taylor,* [2003]; *Taylor and Yin,* [*2009*]; Fault database is from *Styron et al.,* [*2010*].

Figure 2:

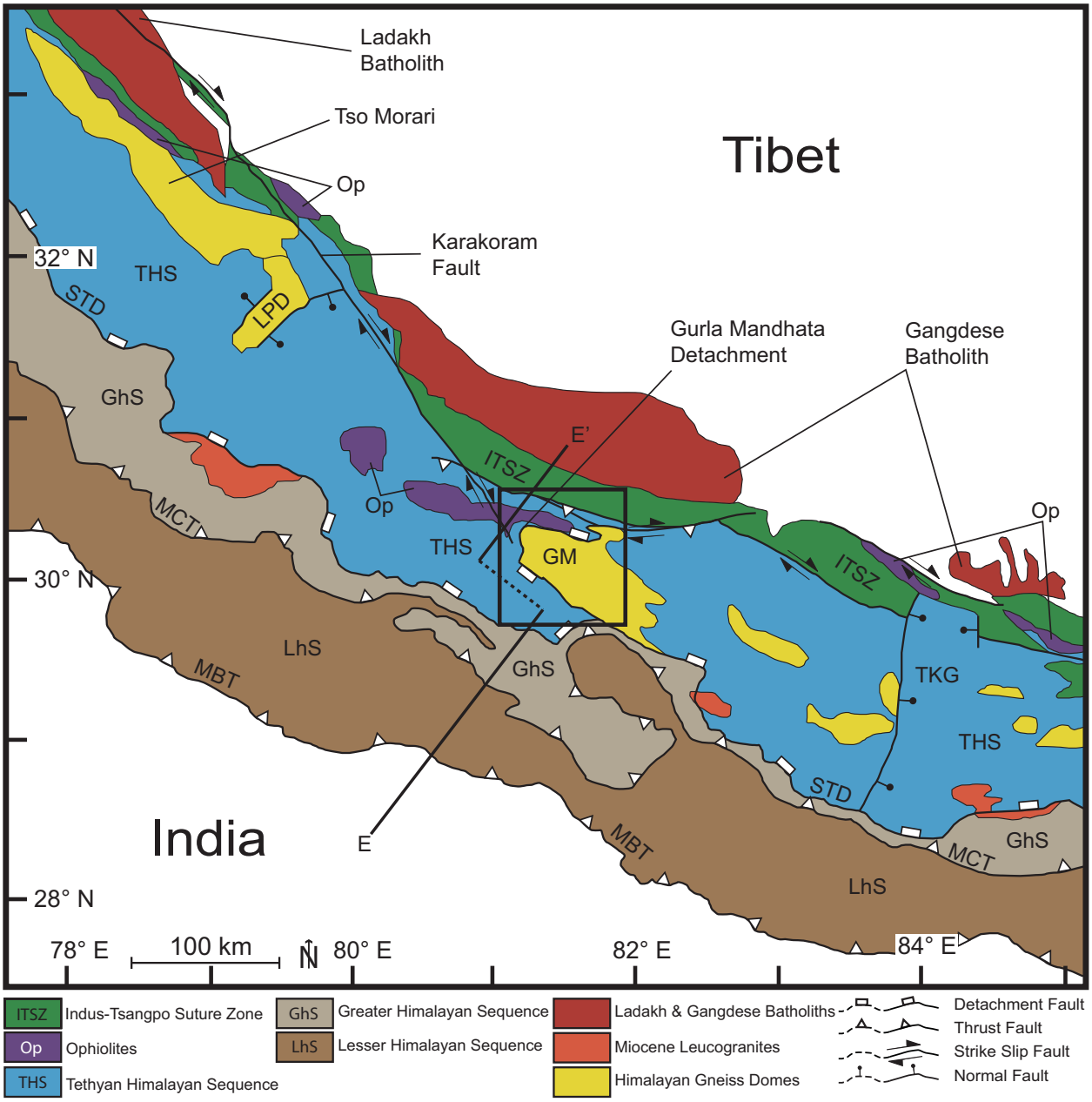
Ladakh
Batholith
Tso Morari
Op
Karakoram
Fault
Tibet
32° N
THS
STD
LPD
GhS
Gurla Mandhata
Detachment
Gangdese
Batholith
E'
ITSZ
Op
MCT
THS
GM
30° N
LhS
MBT
GhS
TKG
THS
STD
India
E
MBT
GhS
MCT
LhS
28° N
78° E
100 km
N
80° E
82° E
84° E
ITSZ Indus-Tsangpo Suture Zone
Op Ophiolites
THS Tethyan Himalayan Sequence
GhS Greater Himalayan Sequence
LhS Lesser Himalayan Sequence
Ladakh & Gangdese Batholiths
Miocene Leucogranites
Himalayan Gneiss Domes
Detachment Fault
Thrust Fault
Strike Slip Fault
Normal Fault

Figure 2:

Generalized regional map of the western Himalaya. Black square indicates the location of Figure 6. The Cross section E-E' is found in Figure 3. GM – Gurla Mandhata; LPD – Leo Pargil Dome; MBT – Main Boundary thrust; MCT – Main Central thrust; STD – South Tibetan detachment; TKG – Takkhola Graben. Figure is modified from *Hodges,* [*2000*]; *Murphy and Copeland,* [*2005*]; *Pullen et al.,* [*2011*].

Figure 3:

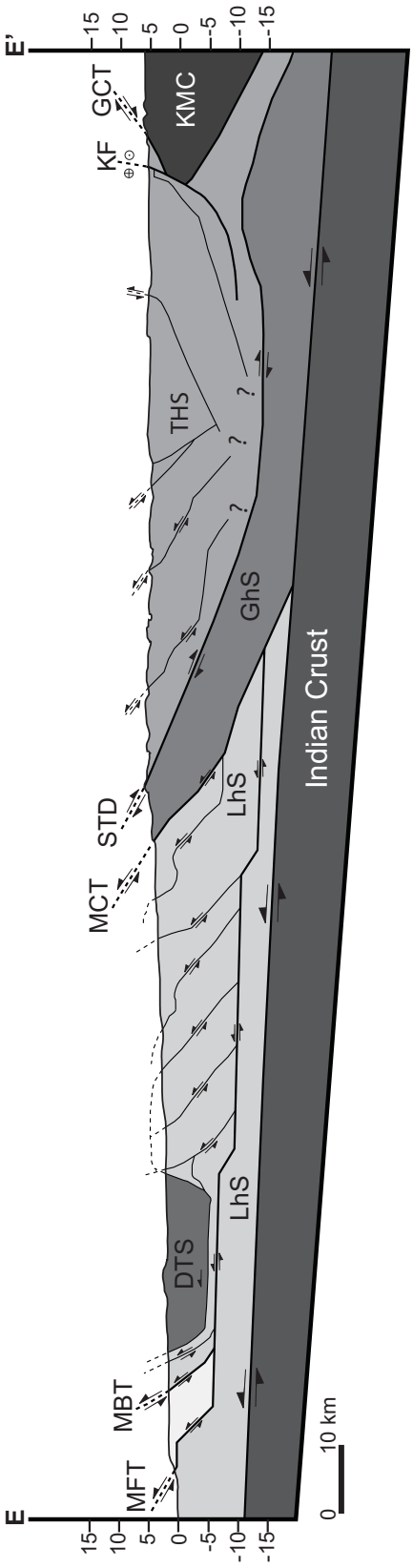
E'
15
10
5
0
-5
-10
-15
GCT
KF
KMC
THS
?
?
?
GhS
Indian Crust
STD
LhS
MCT
LhS
DTS
MBT
MFT
E
15
10
5
0
-5
-10
-15
0
10 km

Figure 3:

Schematic regional cross section of the Himalaya (E-E'; Figure 2). DTS – Dadeldhura thrust sheet; GCT – Great Counter Thrust; GhS – Greater Himalayan Sequence; KF – Karakoram fault; KMC – Kailas Magmatic Complex; LhS – Lesser Himalayan Sequence; MBT – Main Boundary Thrust; MCT – Main Central Thrust; MFT – Main Frontal Thrust; STD – South Tibetan Detachment; THS – Tethyan Himalayan Sequence. Figure modified from *Murphy and Yin,* [*2003*].

Figure 4:

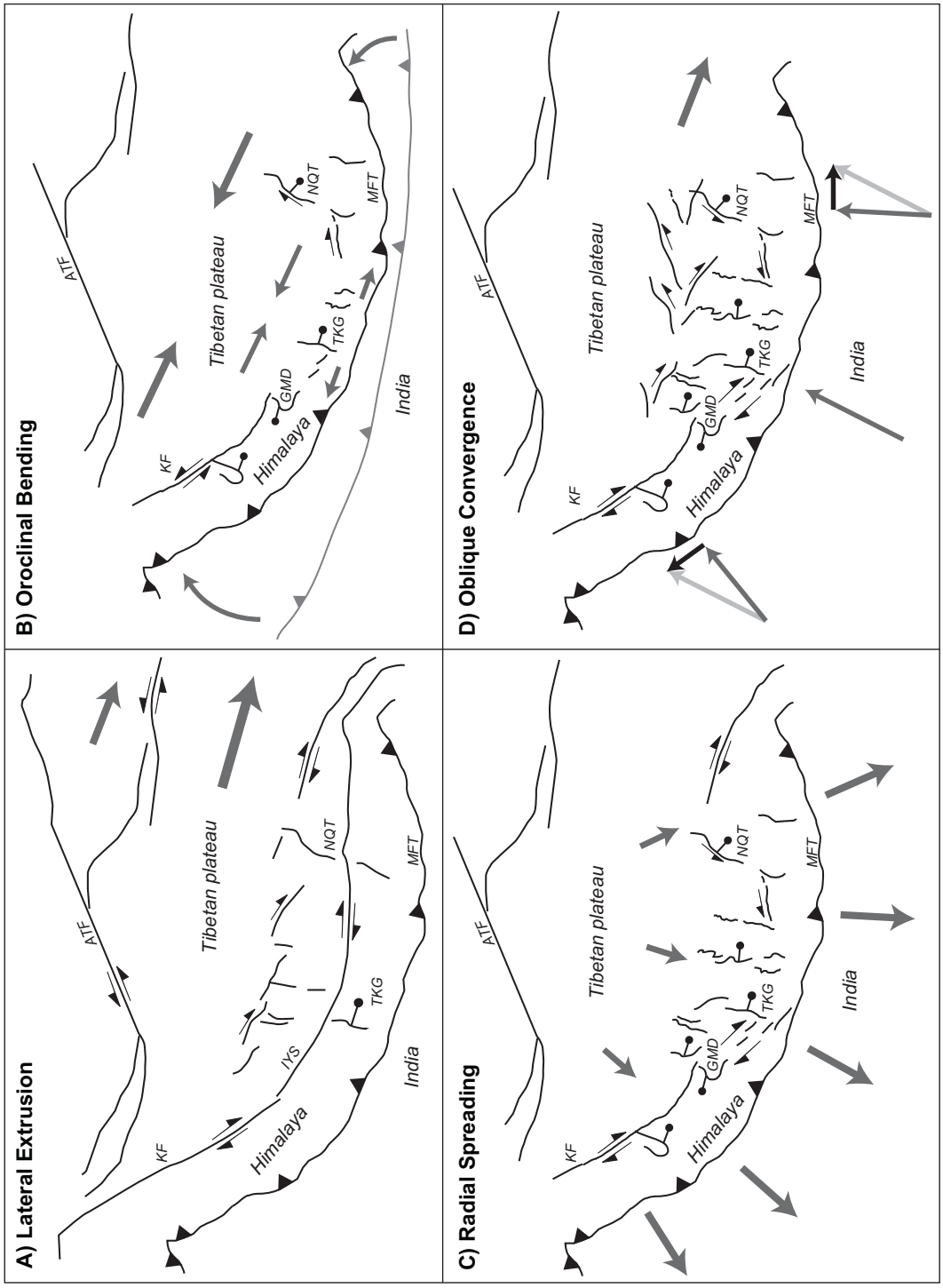
A) Lateral Extrusion
B) Oroclinal Bending
C) Radial Spreading
D) Oblique Convergence
ATF
KF
Tibetan plateau
Himalaya
India
IYS
TKG
GMD
NQT
MFT

Figure 4:

Models of Himalayan and south Tibetan development. (A) Lateral extrusion, (B) oroclinal bending, (C) radial spreading, and (D) oblique convergence. ATF – Altyn Tagh fault; KF – Karakoram fault; GMD – Gurla Mandhata detachment; MFT – Main Frontal Thrust; NQT – Nyainqentanglha Shan; TKG – Takkhola Graben. Figure modified from *Styron et al.,* [*2011*].

Figure 5:

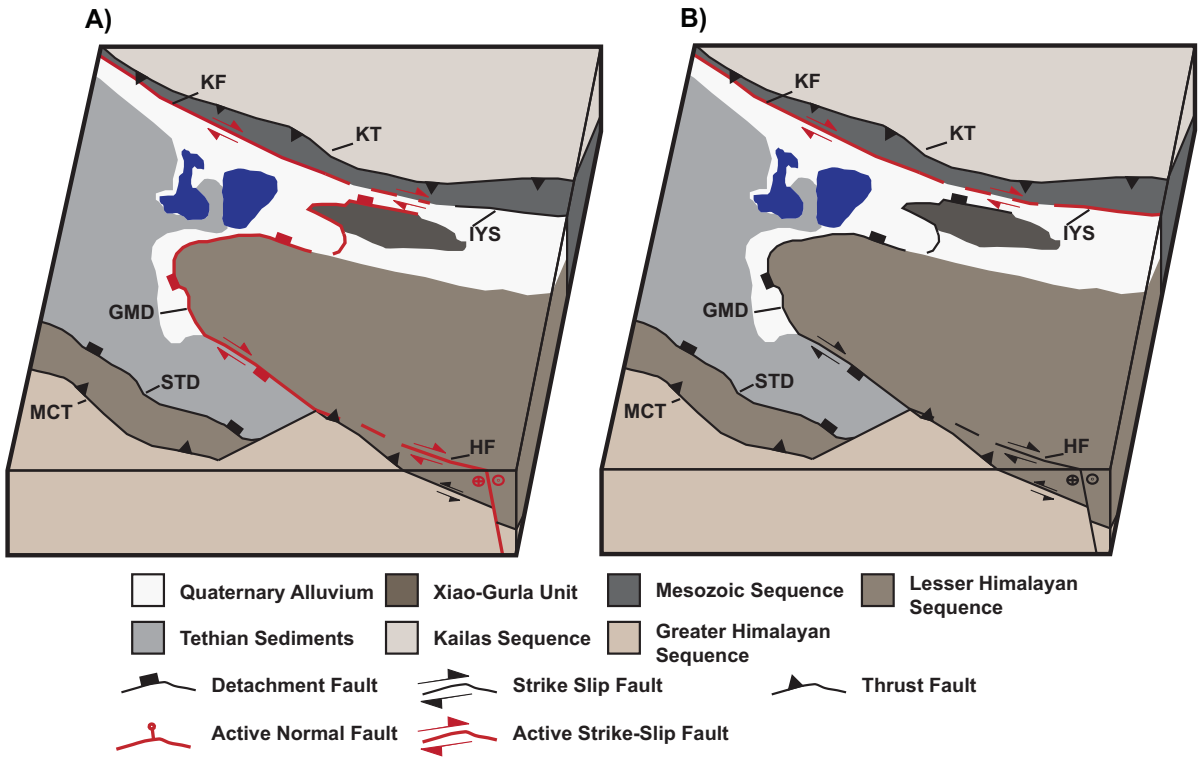
A)
B)
KF
KT
IYS
GMD
STD
MCT
HF
Quaternary Alluvium
Xiao-Gurla Unit
Mesozoic Sequence
Lesser Himalayan Sequence
Tethian Sediments
Kailas Sequence
Greater Himalayan Sequence
Detachment Fault
Strike Slip Fault
Thrust Fault
Active Normal Fault
Active Strike-Slip Fault

Figure 5:

Simplified block models of southwest Tibet showing the different slip transfer paths. (A) Oblique convergence model: Red lines indicate active faults showing the slip propagation predicted by the oblique convergence model. In this model the slip from the Karakoram fault is transferred onto the Gurla Mandhata detachment and continues south, eventually being transferred onto the Humla fault. (B) Lateral extrusion model: Red lines indicate active faults showing the slip propagation predicted by the lateral extrusion model. In this model the slip is transferred from the Karakoram fault directly into the Indus-Yalu Suture bypassing the Gurla Mandhata Detachment. GMD - Gurla Mandhata Detachment; HF - Humla fault; IYS - Indus-Yalu Suture; KF - Karakoram fault; KT - Kailas Thrust; MCT – Main Central Thrust; STD - South Tibetan Detachment.

Figure 6:

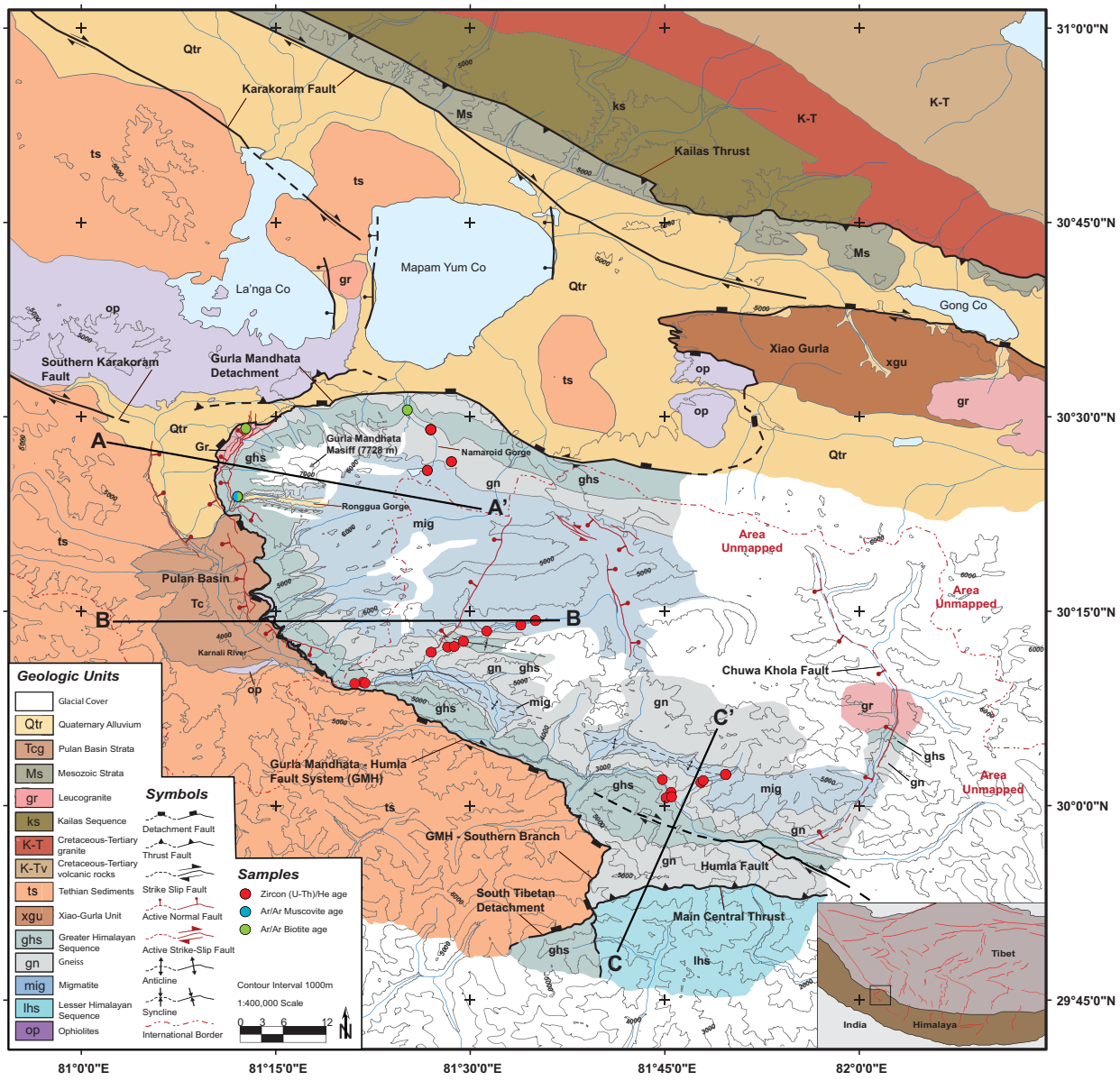
Qtr
Karakoram Fault
Ms
ks
K-T
Kailas Thrust
ts
Mapam Yum Co
La'nga Co
gr
op
Qtr
Gong Co
Xiao Gurla
xgu
Southern Karakoram Fault
Gurla Mandhata Detachment
A
A'
Gr
ghs
Gurla Mandhata Masiff (7728 m)
Namaroid Gorge
gn
Ronggua Gorge
mig
Area Unmapped
Pulan Basin
Tc
B
B'
Karnali River
Chuwa Khola Fault
C
C'
Gurla Mandhata - Humla Fault System (GMH)
GMH - Southern Branch
Humla Fault
South Tibetan Detachment
Main Central Thrust
lhs
Tibet
India
Himalaya
31°0'0"N
30°45'0"N
30°30'0"N
30°15'0"N
30°0'0"N
29°45'0"N
81°0'0"E
81°15'0"E
81°30'0"E
81°45'0"E
82°0'0"E
Geologic Units
Glacial Cover
Quaternary Alluvium
Tcg
Pulan Basin Strata
Mesozoic Strata
Leucogranite
Kailas Sequence
Cretaceous-Tertiary granite
Cretaceous-Tertiary volcanic rocks
Tethian Sediments
Xiao-Gurla Unit
Greater Himalayan Sequence
Gneiss
Migmatite
Lesser Himalayan Sequence
Ophiolites
Symbols
Detachment Fault
Thrust Fault
Strike Slip Fault
Active Normal Fault
Active Strike-Slip Fault
Anticline
Syncline
International Border
Samples
Zircon (U-Th)/He age
Ar/Ar Muscovite age
Ar/Ar Biotite age
Contour Interval 1000m
1:400,000 Scale
0 3 6 12
N

Figure 6:

Simplified geologic map of Gurla Mandhata and surrounding area. Red sample locations indicate zircon (U-Th)/He ages from this study, blue sample locations indicate muscovite $^{40}Ar/^{39}Ar$ data from *Murphy et al.,* [*2002*], and green sample locations indicate biotite $^{40}Ar/^{39}Ar$ data from *Murphy et al.,* [*2002*]. Cross section A-A', B-B', and C-C' are shown. Map location is shown on the inset in the bottom right corner. Modified from *Murphy et al.,* [*2002*]; *Murphy and Copeland,* [*2005*]; *Murphy and Burgess,* [*2006*]; *Pullen et al.,* [*2011*].

Figure 7:

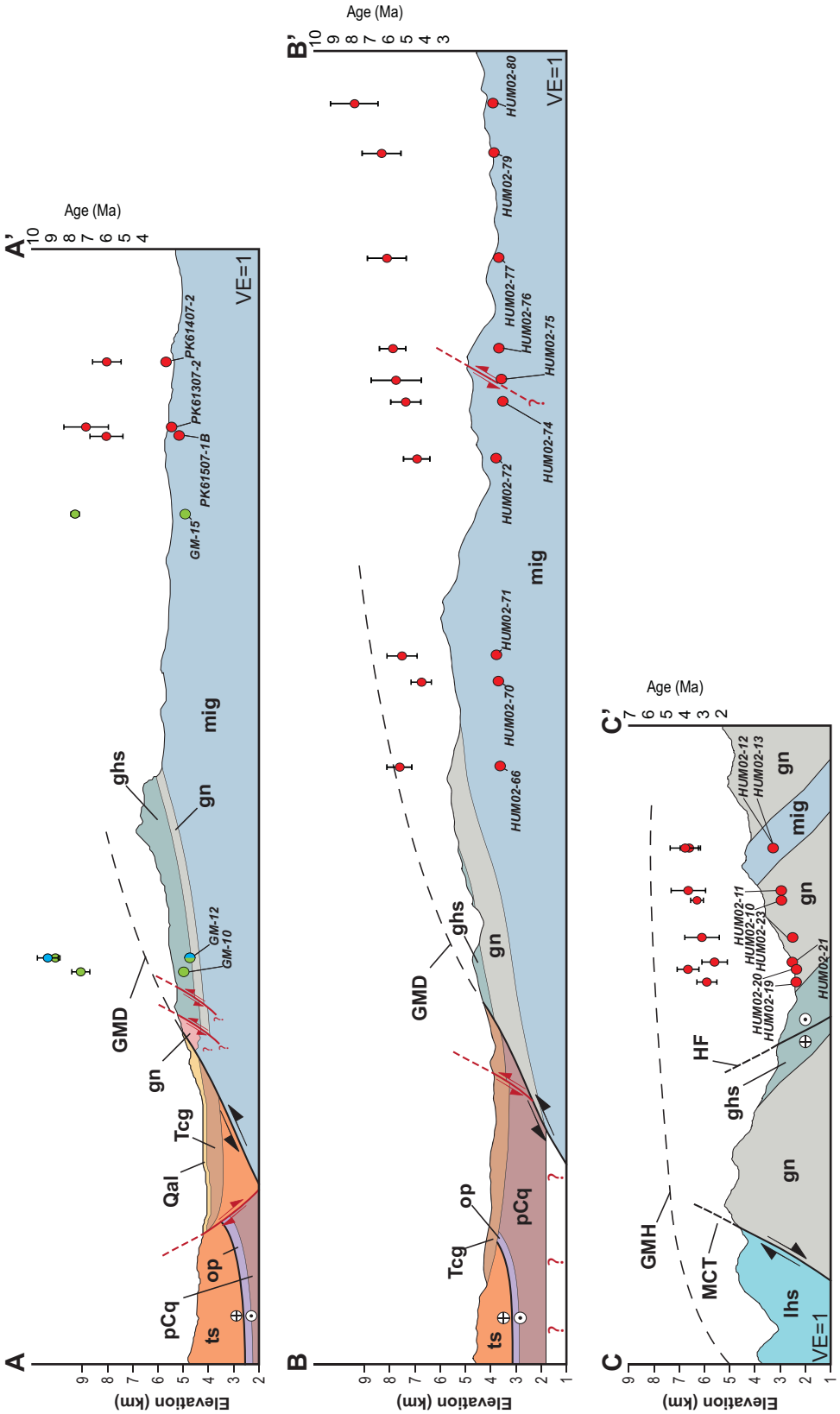
A
A'
B
B'
C
C'
Age (Ma)
Elevation (km)
VE=1
GMD
GMH
MCT
HF
ghs
gn
mig
lhs
Qal
Tcg
op
pCq
ts
GM-15
GM-12
GM-10
PK61507-1B
PK61307-2
PK61407-2
HUM02-66
HUM02-70
HUM02-71
HUM02-72
HUM02-74
HUM02-75
HUM02-76
HUM02-77
HUM02-79
HUM02-80
HUM02-10
HUM02-11
HUM02-12
HUM02-13
HUM02-19
HUM02-20
HUM02-21
HUM02-23

Figure7:

(A) Structural cross section (A-A') of the northern segment of the Gurla Mandhata detachment. Samples are projected into the cross section. Blue sample locations are muscovite $^{40}Ar/^{39}Ar$ data with 2-σ error bars, green sample locations are biotite $^{40}Ar/^{39}Ar$ data with 2-σ error bars. (B) Structural cross section (B-B') of the central segment of the Gurla Mandhata detachment. Samples are projected into the cross section. Red sample locations are zircon (U-Th)/He ages are plotted above the samples with 2-σ error bars. (C) Structural cross section (C-C') of the southern segment of the Gurla Mandhata detachment and Humla fault. Samples are projected into the cross section. $^{40}Ar/^{39}Ar$ data and kinematic data are from *Murphy et al.,* [*2002*]; *Murphy and Copeland,* [*2005*]. GMD – Gurla Mandhata Detachment; GMH – Gurla Mandhata Humla Fault; HF- Humla Fault; MCT – Main Central Thrust.

Figure 8:

A)

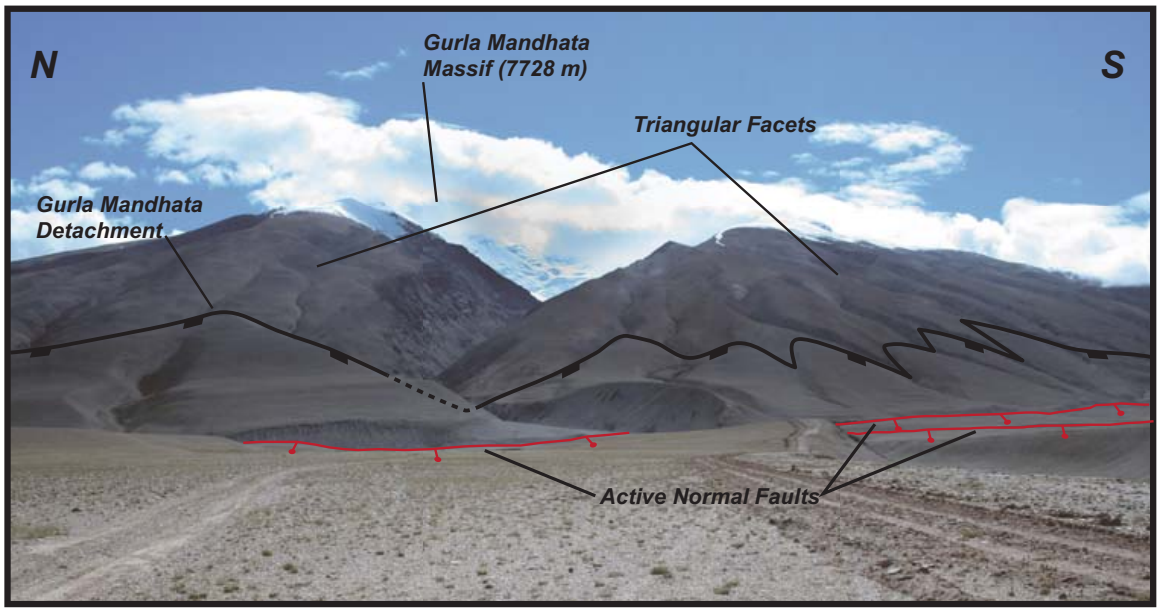
N
S
Gurla Mandhata
Massif (7728 m)
Triangular Facets
Gurla Mandhata
Detachment
Active Normal Faults

B)

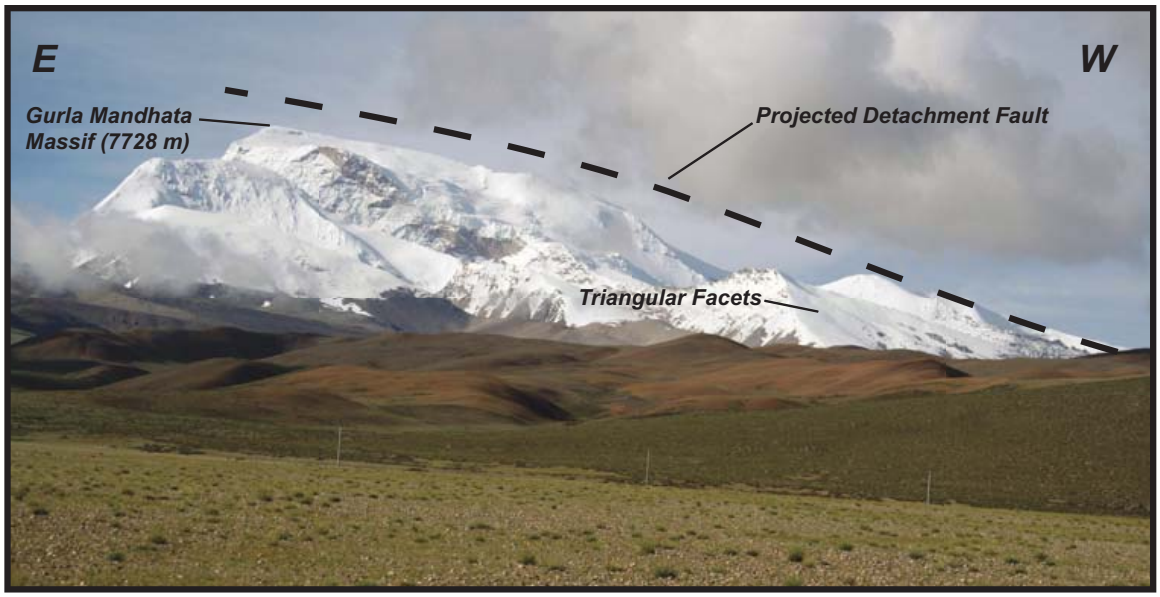
E
W
Gurla Mandhata
Massif (7728 m)
Projected Detachment Fault
Triangular Facets

Figure 8:

(A) East-looking photograph taken in the northern Pulan basin. Red lines mark active normal faults cutting the basin sediments, and dashed black lines mark the trace of Gurla Mandhata Detachment. (B) South-looking photograph of the Gurla Mandhata massif. The dashed black line represents the projected fault trace defined by the main east-west ridge showing shallowing of the fault dip. Photo was taken at ~4000 m.

Figure 9:

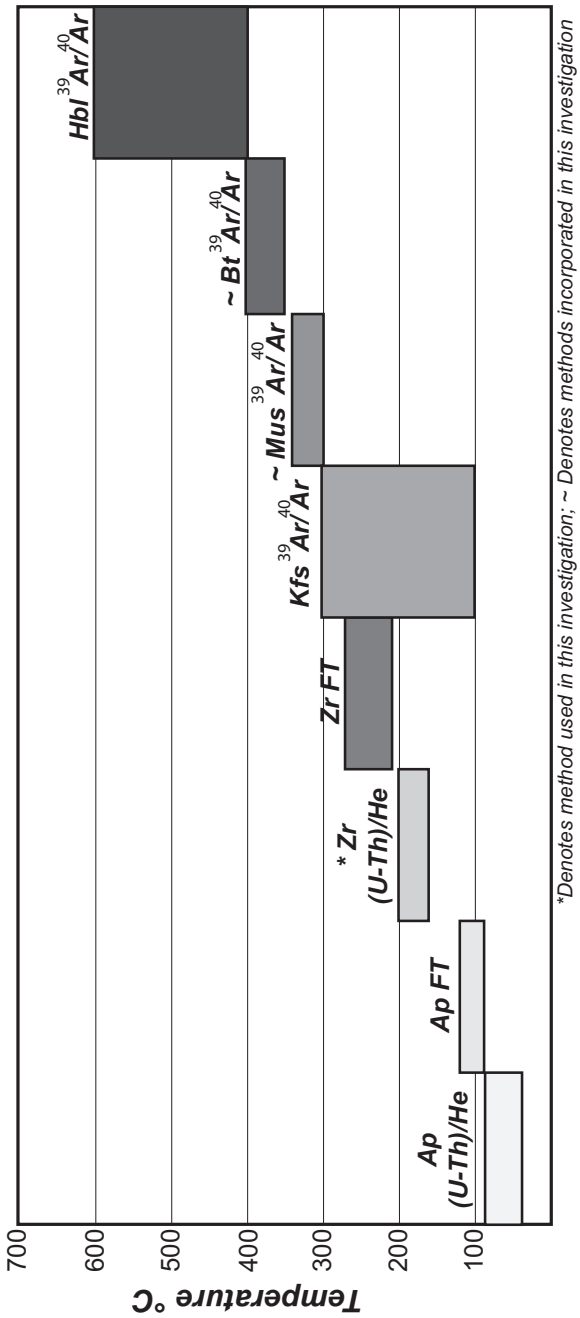
Hbl $^{39}Ar/^{40}Ar$
~ Bt $^{39}Ar/^{40}Ar$
~ Mus $^{39}Ar/^{40}Ar$
Kfs $^{39}Ar/^{40}Ar$
Zr FT
* Zr (U-Th)/He
Ap FT
Ap (U-Th)/He
700
600
500
400
300
200
100
Temperature °C
*Denotes method used in this investigation; ~ Denotes methods incorporated in this investigation

Figure 9:

Plot of different thermochronometers showing their closure temperature ranges. Ap - Apatite; Bt - Biotite; FT - Fission Track; Hbl – Hornblende; Kfs - Potassium Feldspar; Mus - Muscovite; Zr - Zircon. Data from *Brandon et al.,* [*1998*]; *Bernet et al.,* [*2002*]; *Reiners et al.,* [*2002*]; *Tagami et al.,* [*2003*]; *Reiners et al.,* [*2005*]; *Stockli,* [*2005*]; *Wolfe and Stockli,* [*2010*].

Figure 10:

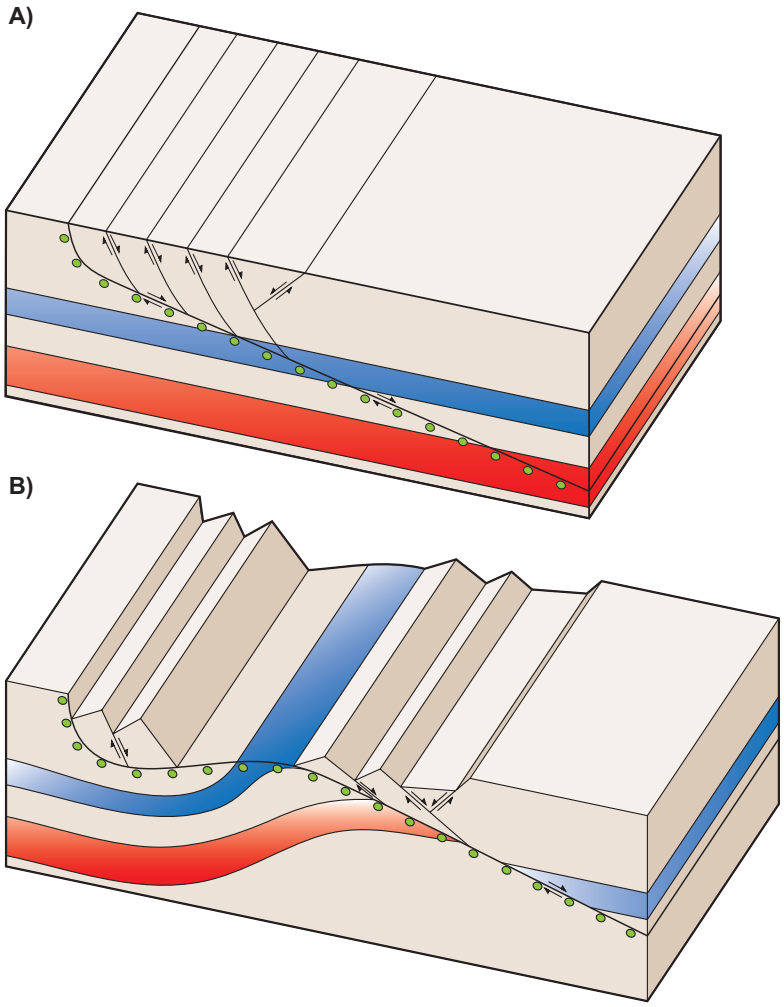

Figure 10:

Block model showing the exhumation of a footwall during slip along a low-angle normal fault. The blue band represents the (U-Th)/He partial retention zone (PRZ) for apatite and the red band is used for the zircon partial retention zone. Green circles indicate the hypothetical footwall sample locations. (A) Shows pre-extension locations of all samples and original geometry of faults. (B) Shows the post-extension fault geometry, sample locations and apatite and zircon partial retention zones. Modified from *Stockli,* [*2005*].

Figure 11:

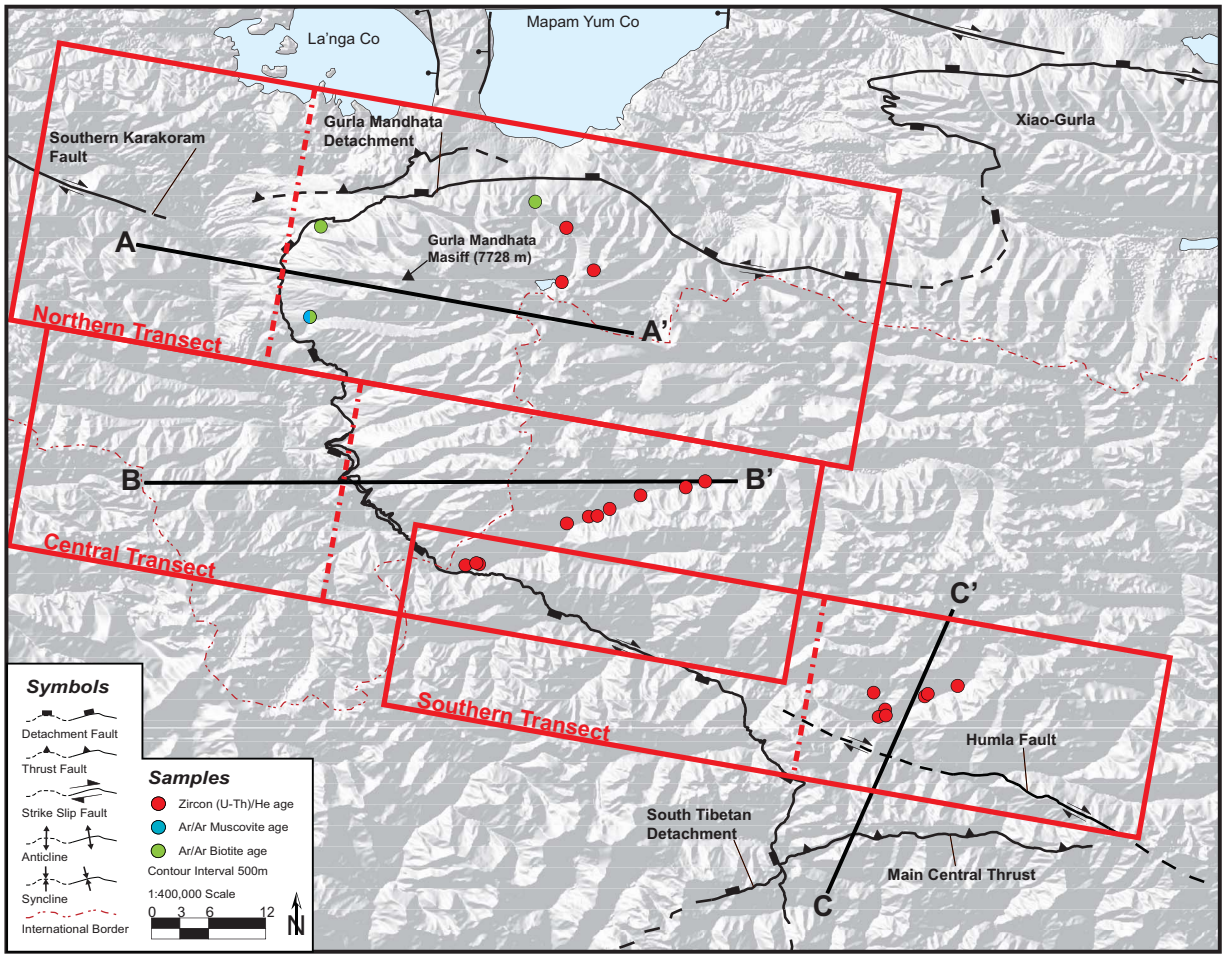
La'nga Co
Mapam Yum Co
Southern Karakoram Fault
Gurla Mandhata Detachment
Xiao-Gurla
Gurla Mandhata Masiff (7728 m)
A
A'
Northern Transect
B
B'
Central Transect
Southern Transect
C'
C
Humla Fault
South Tibetan Detachment
Main Central Thrust
Symbols
Detachment Fault
Thrust Fault
Strike Slip Fault
Anticline
Syncline
International Border
Samples
Zircon (U-Th)/He age
Ar/Ar Muscovite age
Ar/Ar Biotite age
Contour Interval 500m
1:400,000 Scale
0 3 6 12
N

Figure 11:

Hill shade map of the GMD with the major faults shown for reference. Red squares show the location of each of the three PeCube models (northern, central, and southern transects) and their relation to the samples (Red – zircon (U-Th)/He; Blue – muscovite $^{40}Ar/^{39}Ar$; Green – biotite $^{40}Ar/^{39}Ar$) and cross sections (A-A', B-B', and C-C'). Each model has been oriented to the mean slip direction (100°). The dashed red lines in each box show the orientation of the modeled detachment fault within each model.

Figure 12:

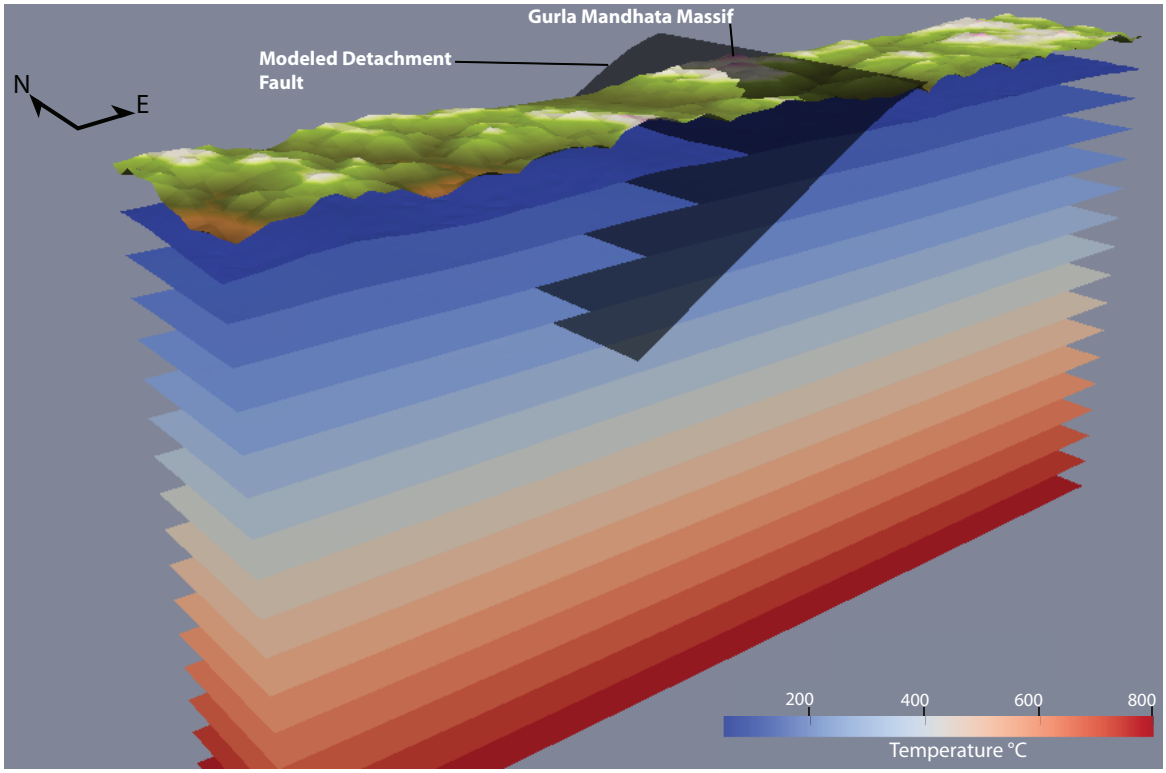
Gurla Mandhata Massif
Modeled Detachment Fault
N
E
200
400
600
800
Temperature °C

Figure 12:

Example of the PeCube model space. The depth shown is 65 km with the subsurface temperature contours at 50 C° intervals. The detachment is shown in black. Note the slight domal curvature of the fault as it is projected above the surface. The surface is a color-shaded relief 90 m DEM with a 15x smoothing factor applied (i.e., changing DEM to 1.3 km resolution).

Figure 13:

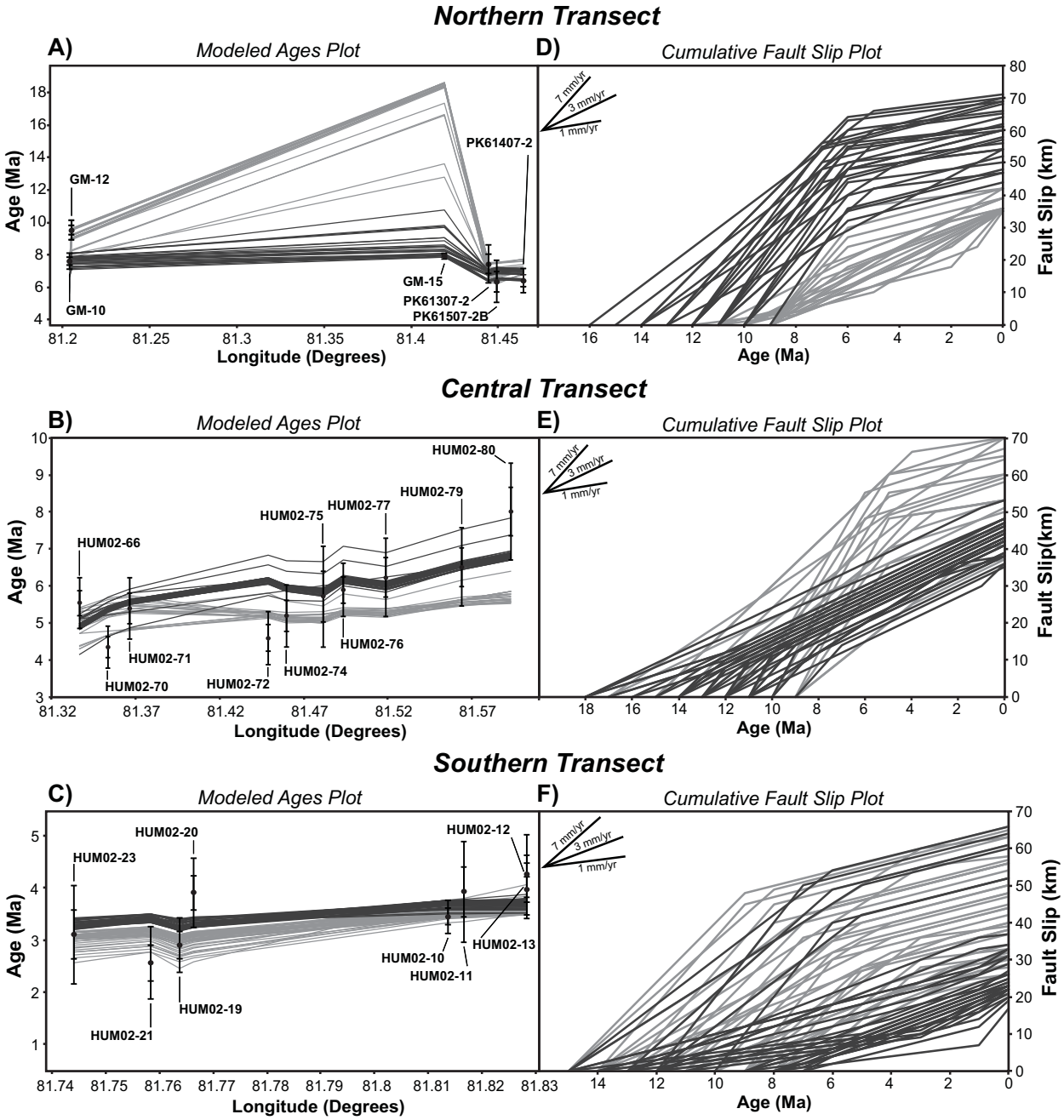
Northern Transect
A)
Modeled Ages Plot
D)
Cumulative Fault Slip Plot
Age (Ma)
Longitude (Degrees)
Fault Slip (km)
Age (Ma)
GM-12
GM-10
GM-15
PK61307-2
PK61507-2B
PK61407-2
7 mm/yr
3 mm/yr
1 mm/yr
Central Transect
B)
Modeled Ages Plot
E)
Cumulative Fault Slip Plot
Age (Ma)
Longitude (Degrees)
Fault Slip(km)
Age (Ma)
HUM02-66
HUM02-71
HUM02-70
HUM02-72
HUM02-74
HUM02-75
HUM02-77
HUM02-76
HUM02-79
HUM02-80
7 mm/yr
3 mm/yr
1 mm/yr
Southern Transect
C)
Modeled Ages Plot
F)
Cumulative Fault Slip Plot
Age (Ma)
Longitude (Degrees)
Fault Slip (km)
Age (Ma)
HUM02-23
HUM02-20
HUM02-21
HUM02-19
HUM02-10
HUM02-11
HUM02-12
HUM02-13
7 mm/yr
3 mm/yr
1 mm/yr

Figure 13:

Zircon (U-Th)/He data results (data points) with PeCube modeling results (lines). Data points are mean sample ages with 1-σ and 2-σ errors. (A) Modeled age plot for the northern transect. Best fit data are in dark grey. (B) Modeled age plot for the central transect. Best fit data are in dark grey. (C) Modeled age data plot for the southern transect. Sample HUM02-20 data are in dark grey while sample HUM02-21 data are in light grey. (D) Cumulative extension for the northern transect. Best fit data are in dark grey. (E) Cumulative extension for the central transect. Best fit data are in the dark grey. (F) Cumulative extension for the southern transect. Sample HUM02-20 data are in dark grey while sample HUM02-21 data are in light grey. See text for a more detailed discussion.

Figure 14:

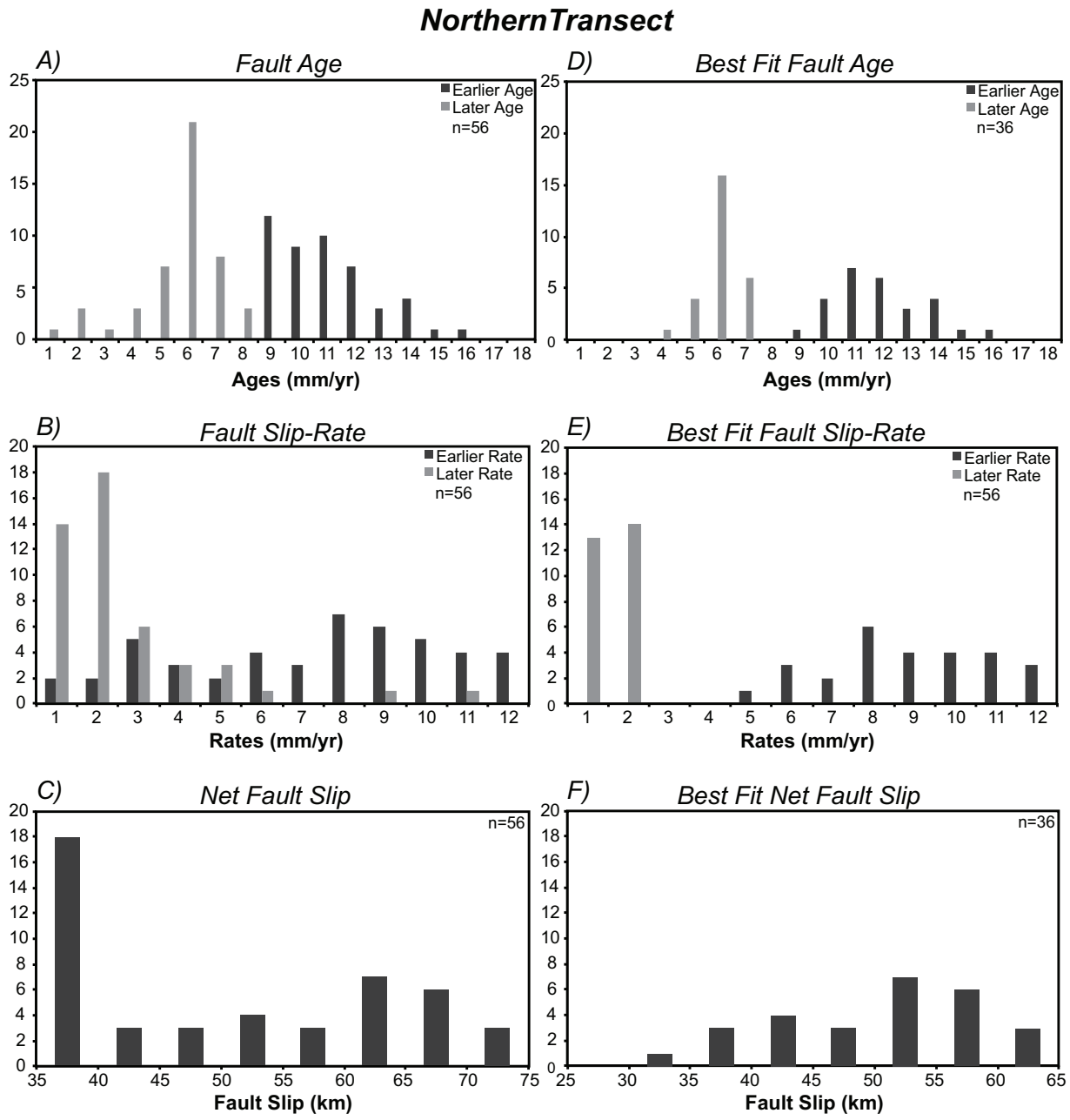
NorthernTransect
A)
Fault Age
Earlier Age
Later Age
n=56
Ages (mm/yr)
D)
Best Fit Fault Age
Earlier Age
Later Age
n=36
Ages (mm/yr)
B)
Fault Slip-Rate
Earlier Rate
Later Rate
n=56
Rates (mm/yr)
E)
Best Fit Fault Slip-Rate
Earlier Rate
Later Rate
n=56
Rates (mm/yr)
C)
Net Fault Slip
n=56
Fault Slip (km)
F)
Best Fit Net Fault Slip
n=36
Fault Slip (km)

Figure 14:

PeCube model results for the northern transect. Dark grey bars represent initiation parameters, light grey bars represent acceleration / post-acceleration parameters. (A) Plot comparing the predicted initiation age to the acceleration age. (B) Comparison of the predicted initiation slip-rate (dark grey) to the post acceleration fault slip-rate (light grey). (C) Predicted net extension for the GMD. Best fit data are the model runs that do not overestimate sample GM-15, as described in section 4.2. (D) Comparison for the best fit fault initiation age to the acceleration age. (E) Comparison of the best fit fault initiation slip-rate (dark grey) to the post acceleration fault slip-rate (light grey). (F) Best fit net extension across the GMD. See text for a more detailed discussion.

Figure 15:

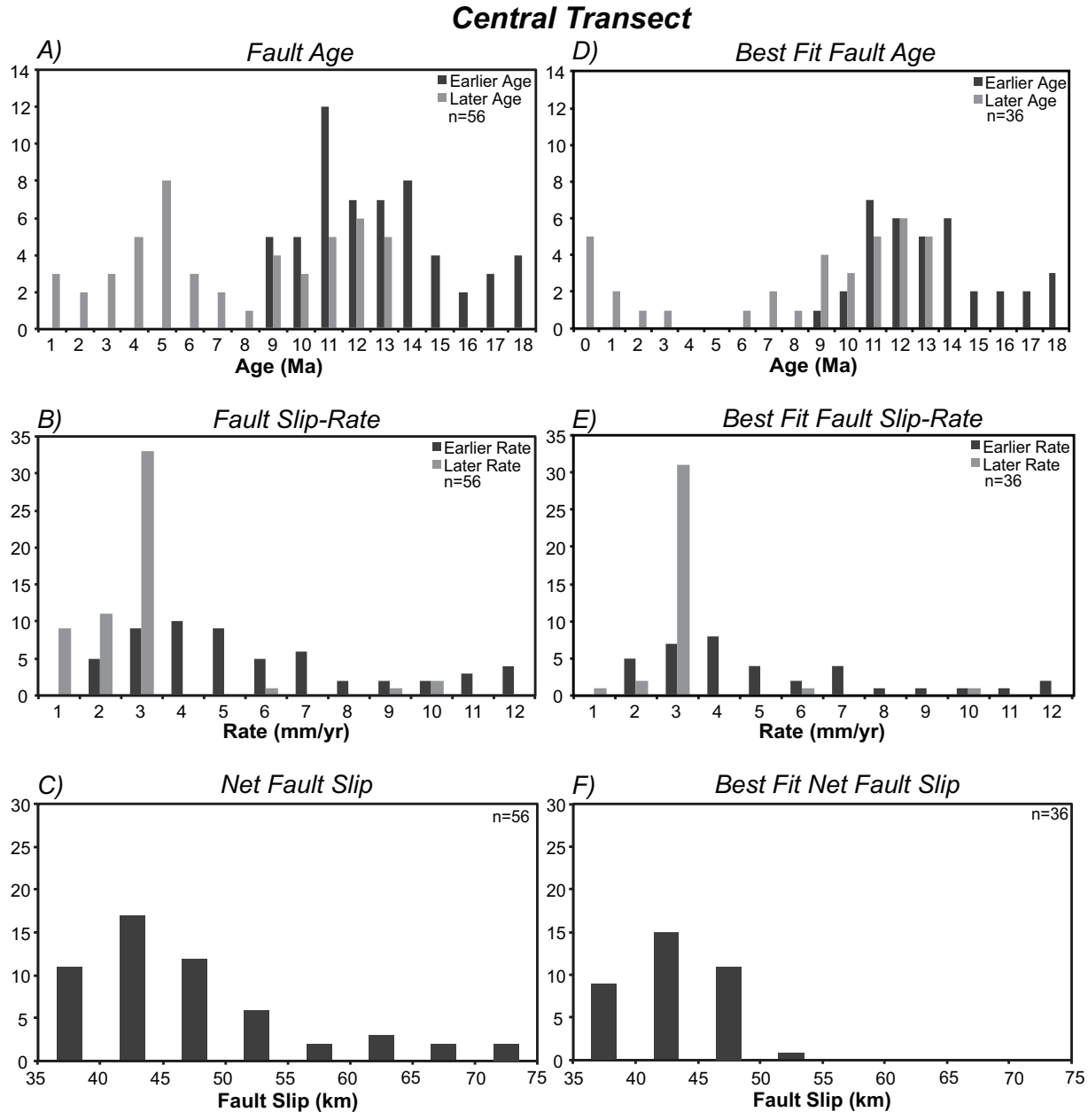
Central Transect
A)
Fault Age
Earlier Age
Later Age
n=56
Age (Ma)
D)
Best Fit Fault Age
Earlier Age
Later Age
n=36
Age (Ma)
B)
Fault Slip-Rate
Earlier Rate
Later Rate
n=56
Rate (mm/yr)
E)
Best Fit Fault Slip-Rate
Earlier Rate
Later Rate
n=36
Rate (mm/yr)
C)
Net Fault Slip
n=56
Fault Slip (km)
F)
Best Fit Net Fault Slip
n=36
Fault Slip (km)

Figure 15:

PeCube model results for the central transect. Dark grey bars represent fault initiation parameters, light grey bars represent acceleration and post-acceleration parameters. (A) Comparison of the predicted fault initiation age to the acceleration age. (B) Comparison of the predicted initiation slip-rate (dark grey) to the post acceleration slip-rate (light grey). (C) Net extension across the GMD. Best fit data are the model runs that are able to capture sample HUM02-80, as described in section 4.3. (D) Comparing of the best fit fault initiation age to the acceleration age. (E) Comparison of the best fit initiation slip-rate (dark grey) to the post acceleration slip-rate (light grey). (F) Best fit net extension across the GMD.

Figure 16:

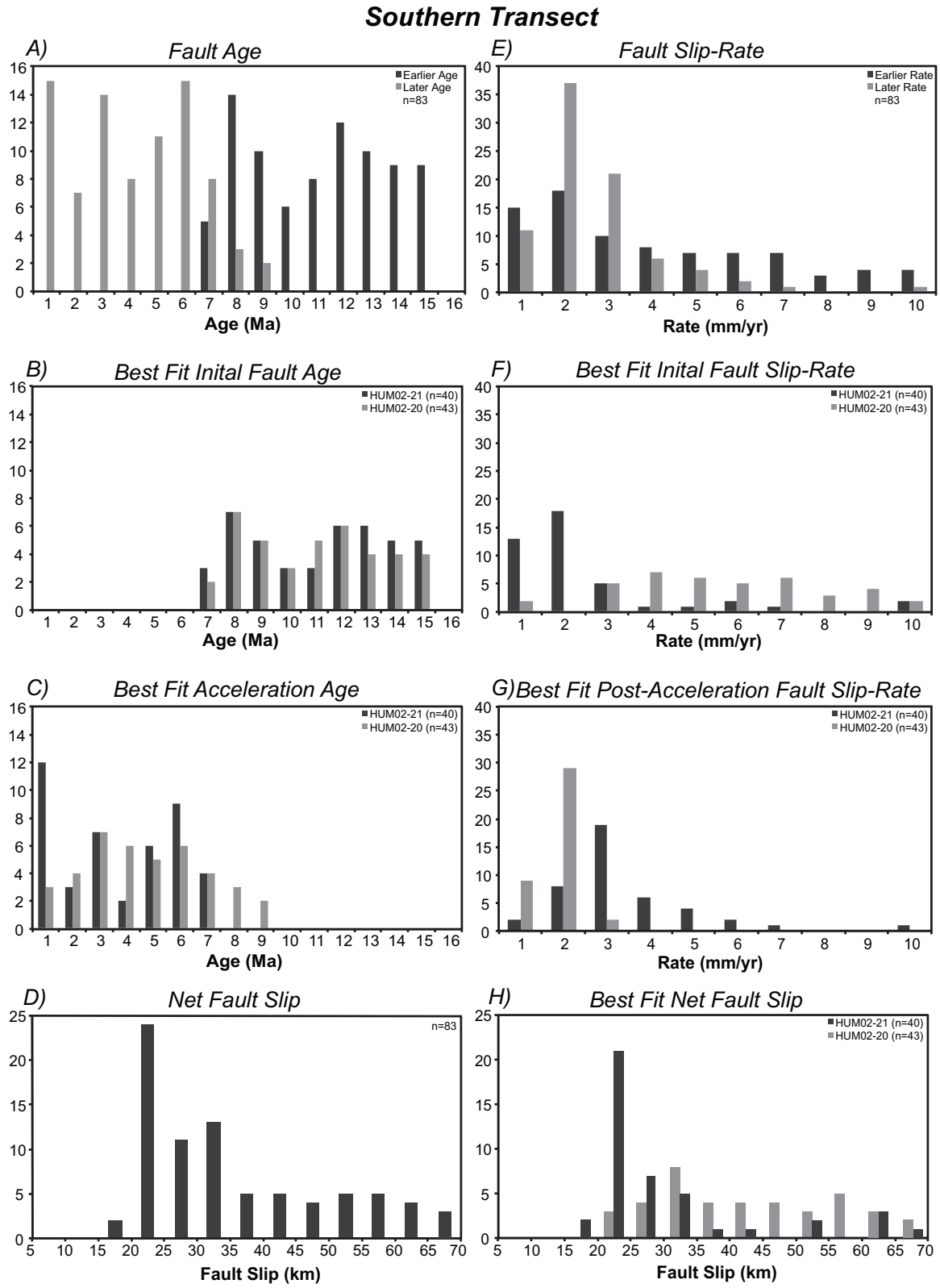
Southern Transect
A)
Fault Age
Earlier Age
Later Age
n=83
Age (Ma)
E)
Fault Slip-Rate
Earlier Rate
Later Rate
n=83
Rate (mm/yr)
B)
Best Fit Inital Fault Age
HUM02-21 (n=40)
HUM02-20 (n=43)
Age (Ma)
F)
Best Fit Inital Fault Slip-Rate
HUM02-21 (n=40)
HUM02-20 (n=43)
Rate (mm/yr)
C)
Best Fit Acceleration Age
HUM02-21 (n=40)
HUM02-20 (n=43)
Age (Ma)
G)
Best Fit Post-Acceleration Fault Slip-Rate
HUM02-21 (n=40)
HUM02-20 (n=43)
Rate (mm/yr)
D)
Net Fault Slip
n=83
Fault Slip (km)
H)
Best Fit Net Fault Slip
HUM02-21 (n=40)
HUM02-20 (n=43)
Fault Slip (km)

Figure 16:

PeCube model results for the southern transect. (A) Comparison of the predicted initiation (dark grey) age to the acceleration age (light grey). (B) Comparison of the HUM02-20 initiation age (dark grey) to the HUM02-21 initiation age (light grey). (C) Comparison of the HUM02-20 acceleration age (dark grey) to the HUM02-21 acceleration age (light grey). (D) Predicted net extension across the GMD. (E) Comparison of the predicted initiation slip-rate (dark grey) to the post acceleration slip-rate (light grey). (F) Comparison of the HUM02-20 initiation slip-rate (dark grey) to the HUM02-21 initiation slip-rate (light grey). (G) Comparison of the HUM02-20 post-acceleration slip-rate (dark grey) to the HUM02-21 post-acceleration slip-rate (light grey). (H) Comparison of the HUM02-20 net extension (dark grey) to the HUM02-21 net extension (light grey).

Figure 17:

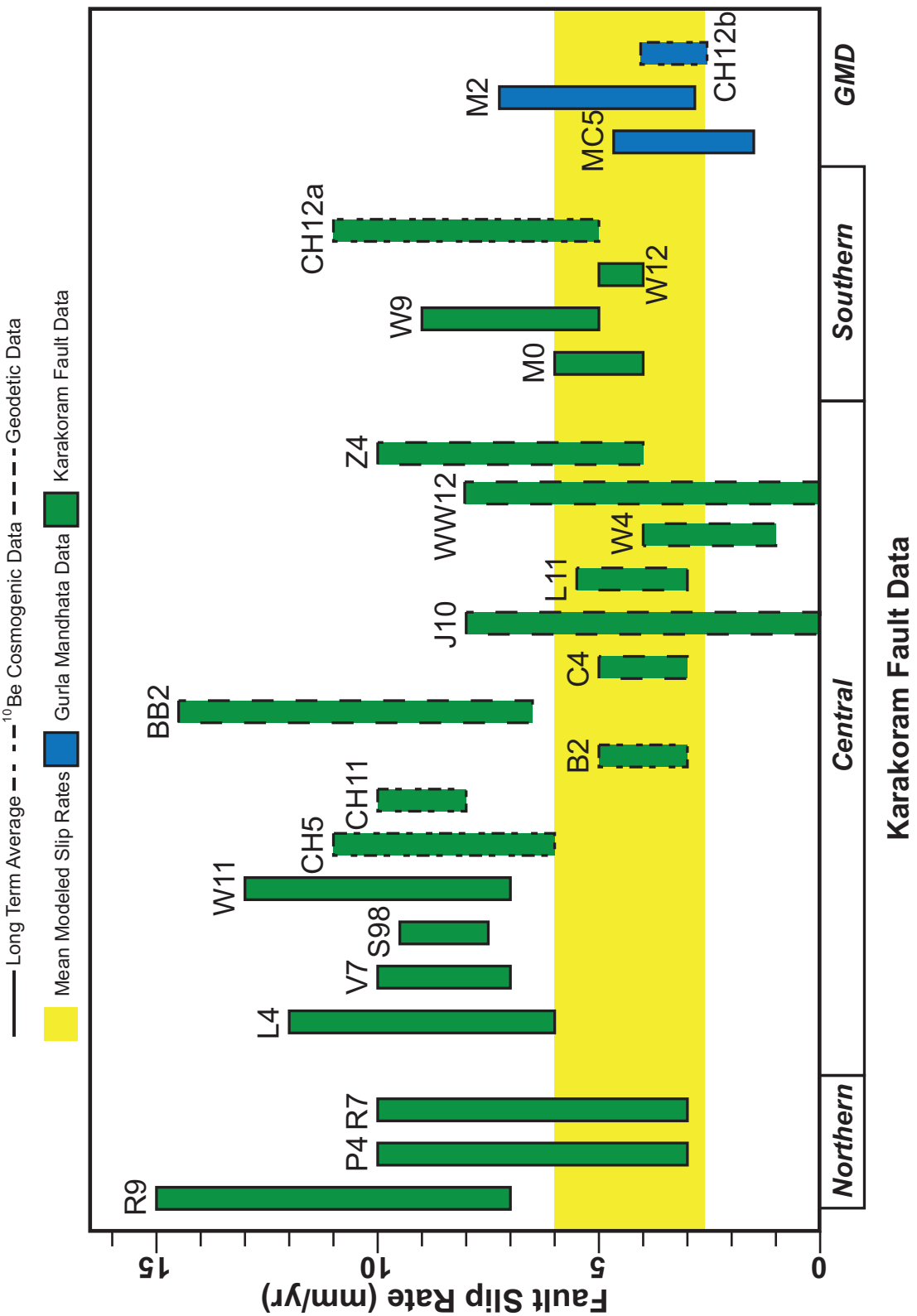
Long Term Average
10Be Cosmogenic Data
Geodetic Data
Mean Modeled Slip Rates
Gurla Mandhata Data
Karakoram Fault Data
Fault Slip Rate (mm/yr)
0
5
10
15
Northern
Central
Southern
GMD
Karakoram Fault Data
R9
P4
R7
L4
V7
S98
W11
CH5
CH11
BB2
B2
C4
J10
L11
W4
WW12
Z4
M0
W9
CH12a
W12
M2
MC5
CH12b

Figure 17:

Comparison of fault slip-rate estimates for the KF and GMD. Blue bars denote data for the GMD, green bars are data for the KF, and Yellow bar represents the mean slip-rates of the three models. Data representing the long-term slip rate have a solid boarder, cosmogenic data have a stippled boarder, and GPS data have a dashed boarder. The data are organized based on their geographic location for each fault. The Karakoram Fault data are organized into three groups: northern data, central data, and southern data. Within each group the data are organized from 10^6-10^1 time scales. The references for the data can be found in Table 4. B2 - *Brown et al.,* [*2002*]; BB2 - *Banerjee and Burgmann,* [*2002*]; C4 - *Chen et al.,* [*2004*]; CH11 - *Chevalier et al.,* [*2011*]; CH12a - *Chevalier et al.,* [*2012a*]; CH12b - *Chevalier et al.,* [*2012b*]; J10 - *Jade et al.,* [*2004, 2010*]; L4 – *Lacassin et al.,* [*2004*]; L11 - *Loveless and Meade,* [*2011*]; M0 - *Murphy et al.,* [*2000*]; M2 - *Murphy et al.,* [*2002*]; M5 - *Murphy and Copeland,* [*2005*]; P4 – *Phillips et al.,* [*2004*]; R7 - *Rutter et al.,* [*2007*]; R9 – *Robinson et al.,* [*2009*]; S98 - *Searle et al.,* [*1998*]; V7 - Valli et al., [*2007, 2008*]; W4 - *Wright et al.,* [*2004*]; W11 - *Wang et al.,* [*2011*]; W12 - *Wang et al.,* [*2012*]; WW12 – *Wang and Wright,* [*2012*]; Z4 - *Zhang et al.,* [*2004*].

Figure 18:

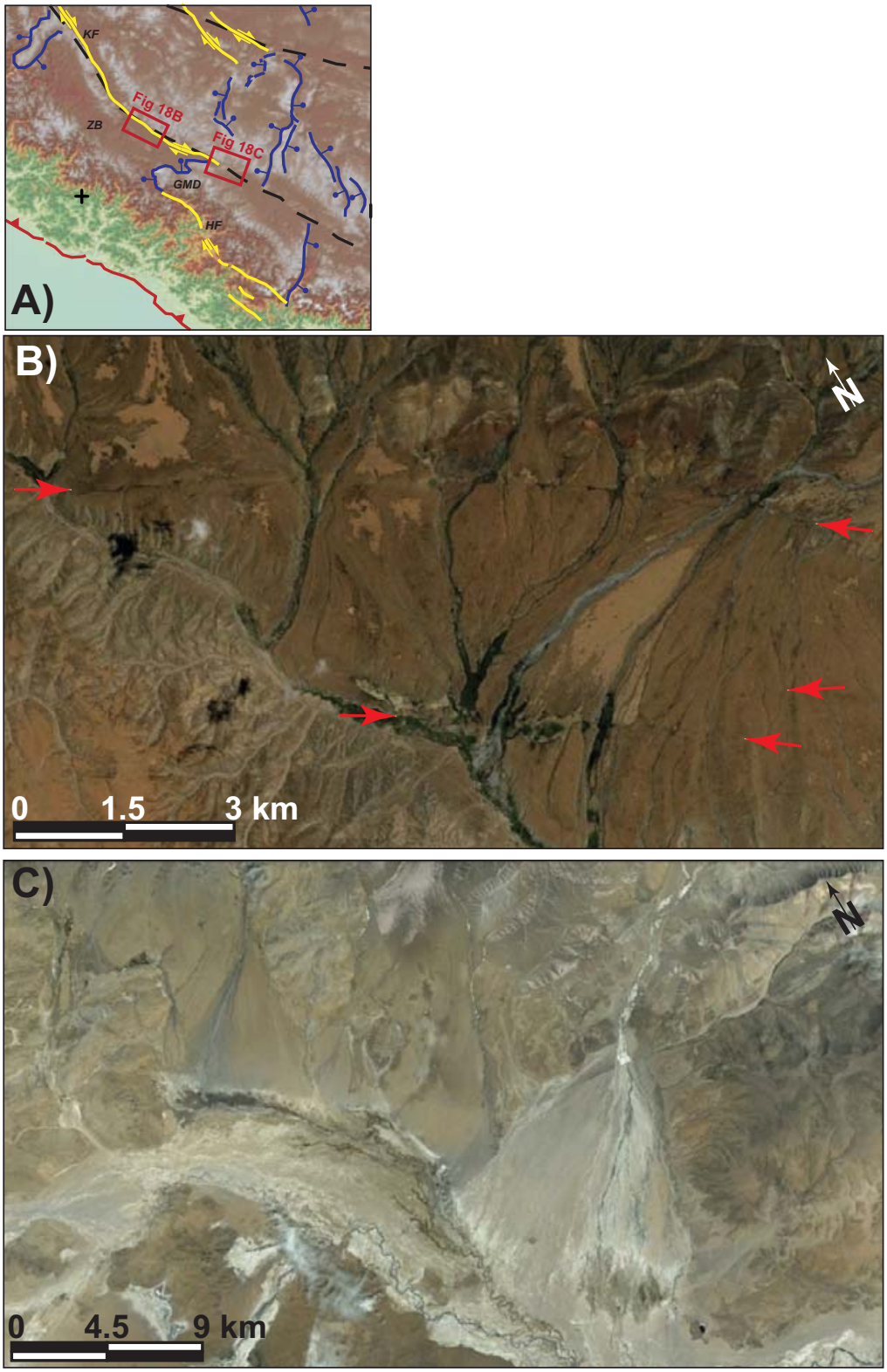

Figure 18:

(A) Shaded relief map of the Tibetan plateau showing the major fault distributions. Thrust faults are in red, normal faults in blue and strike-slip faults in yellow. The dashed black lines represent the suture zones. The red boxes mark the locations for Figure 18B and 18C. GMD – Gurla Mandhata Detachment; HF – Humla fault; KF – Karakoram fault; ZB – Zada Basin. Modified after *Taylor,* [*2003*]; *Taylor and Yin,* [*2009*]; Faults taken from Styron, [2010]. (B) Image of the Karakoram fault north of the Kailas Thrust. Note the offset river terraces and fluvial channels. Image taken from Google Earth. (C) Satellite image southwest of the GMD where the IYS is interpreted to be. Note the lack of active fault traces and there are no apparent offsets of the alluvial fans and active river systems. Image taken from Google Earth.

Table 1:

Reduced (U-Th[Sm])/He Data																		
Sample	**Mineral**	**Unit / Lithology**	**Latitude**	**Longitude**	**Elevation (m)**	**Age, Ma**	**err., Ma**	**U (ppm)**	**Th (ppm)**	**147Sm (ppm)**	**[U]e**	**Th/U**	**He (nmol/g)**	**mass (ug)**	**Ft**	**ESR**	**Average Age (Ma)**	**Age err. (Ma)**
Southern Transect																		
HUM02-10		***gn***																
zHUM02-10-1	zircon	Gneiss	81.81368	30.03698	2900	3.45	0.28	271.3	101.7	2.0	294.7	0.38	4.1	6.04	0.75	47.28		
zHUM02-10-2	zircon	Gneiss	81.81368	30.03698	2900	3.38	0.27	266.4	100.6	2.3	289.6	0.38	4.1	6.84	0.77	50.50		
zHUM02-10-3	zircon	Gneiss	81.81368	30.03698	2900	3.47	0.28	416.3	158.1	1.7	452.7	0.38	6.7	7.72	0.78	54.58		
zHUM02-10-4	zircon	Gneiss	81.81368	30.03698	2900	3.49	0.28	357.0	103.2	1.7	380.7	0.29	5.2	4.10	0.73	42.31		
																	3.45	0.32
HUM02-11		***gn***																
zHUM02-11-1	zircon	Gneiss	81.81655	30.03767	2900	3.87	0.31	198.6	79.5	1.4	216.9	0.40	3.2	2.58	0.71	38.73		
zHUM02-11-2	zircon	Gneiss	81.81655	30.03767	2900	4.44	0.36	525.5	217.6	6.4	575.6	0.41	10.5	4.92	0.76	48.02		
zHUM02-11-3	zircon	Gneiss	81.81655	30.03767	2900	2.81	0.22	130.2	50.4	0.3	141.8	0.39	1.5	2.22	0.68	35.85		
zHUM02-11-4	zircon	Gneiss	81.81655	30.03767	2900	4.15	0.33	312.3	123.5	1.5	340.7	0.40	5.8	5.41	0.76	48.29		
zHUM02-11-5	zircon	Gneiss	81.81655	30.03767	2900	4.35	0.35	438.0	142.7	3.8	470.8	0.33	8.8	9.41	0.80	58.66		
																	3.92	0.97
HUM02-12		***mig***																
zHUM02-12-1	zircon	Gneiss	81.82827	30.04433	3200	4.02	0.32	842.6	272.4	3.6	905.3	0.32	14.8	4.72	0.75	46.53		
zHUM02-12-2	zircon	Gneiss	81.82827	30.04433	3200	4.21	0.34	394.5	179.6	7.6	435.8	0.46	7.8	7.49	0.78	54.88		
zHUM02-12-3	zircon	Gneiss	81.82827	30.04433	3200	3.77	0.30	496.5	184.7	7.5	539.1	0.37	8.3	5.02	0.75	47.34		
zHUM02-12-4	zircon	Gneiss	81.82827	30.04433	3200	4.88	0.39	496.4	128.6	1.1	526.0	0.26	11.2	9.75	0.81	60.81		
																	4.22	0.81
HUM02-13		***mig***																
zHUM02-13-1	zircon	Gneiss	81.82833	30.04425	3190	4.23	0.34	250.6	124.6	3.9	279.3	0.50	5.0	7.45	0.79	55.14		
zHUM02-13-2	zircon	Gneiss	81.82833	30.04425	3190	3.72	0.30	296.6	143.8	3.1	329.8	0.48	5.4	13.29	0.82	65.69		
zHUM02-13-3	zircon	Gneiss	81.82833	30.04425	3190	3.94	0.32	436.7	195.7	3.1	481.7	0.45	7.3	3.39	0.71	39.74		
zHUM02-13-4	zircon	Gneiss	81.82833	30.04425	3190	4.01	0.32	349.7	165.2	2.6	387.8	0.47	6.4	6.37	0.77	50.56		
zHUM02-13-5	zircon	Gneiss	81.82833	30.04425	3190	3.96	0.32	366.4	196.5	4.2	411.6	0.54	6.7	5.66	0.76	49.57		
																	3.97	0.50
HUM02-19		***ghs***																
zHUM02-19-1	zircon	Gneiss	81.76380	30.00432	2410	2.60	0.21	832.2	629.6	2.7	977.1	0.76	10.3	4.55	0.75	46.83		
zHUM02-19-2	zircon	Gneiss	81.76380	30.00432	2410	2.84	0.23	1056.6	763.9	2.3	1232.5	0.72	14.5	6.03	0.77	50.69		
zHUM02-19-3	zircon	Gneiss	81.76380	30.00432	2410	3.29	0.26	917.6	638.5	2.4	1064.6	0.70	13.5	3.62	0.71	40.67		
zHUM02-19-4	zircon	Gneiss	81.76380	30.00432	2410	3.09	0.25	541.3	421.0	3.1	638.2	0.78	8.0	5.02	0.75	47.22		
zHUM02-19-5	zircon	Gneiss	81.76380	30.00432	2410	2.67	0.21	1109.9	783.0	2.7	1290.2	0.71	13.6	3.69	0.73	43.10		
																	2.90	0.52
HUM02-20		***gn***																
zHUM02-20-1	zircon	Gneiss	81.76645	30.00680	2430	3.99	0.32	371.9	26.5	0.3	378.0	0.07	6.8	14.24	0.83	69.95		
zHUM02-20-2	zircon	Gneiss	81.76645	30.00680	2430	4.45	0.36	457.1	95.7	0.9	479.1	0.21	8.7	5.39	0.76	47.18		
zHUM02-20-3	zircon	Gneiss	81.76645	30.00680	2430	3.89	0.31	569.7	31.2	0.4	576.9	0.05	9.2	5.03	0.76	47.21		
zHUM02-20-4	zircon	Gneiss	81.76645	30.00680	2430	3.64	0.29	309.8	34.4	0.5	317.7	0.11	5.1	10.73	0.81	61.12		
zHUM02-20-5	zircon	Gneiss	81.76645	30.00680	2430	3.56	0.28	616.2	23.9	0.3	621.7	0.04	9.1	5.36	0.76	47.45		
																	3.91	0.66
HUM02-21		***gn***																
zHUM02-21-1	zircon	Schist	81.75845	30.01709	2520	2.67	0.21	1841.8	611.0	1.7	1982.4	0.33	20.3	2.86	0.71	39.54		
zHUM02-21-2	zircon	Schist	81.75845	30.01709	2520	2.00	0.16	518.1	124.1	4.8	546.6	0.24	4.2	2.73	0.71	39.17		
zHUM02-21-3	zircon	Schist	81.75845	30.01709	2520	3.17	0.25	1563.3	779.2	2.1	1742.7	0.50	22.2	4.66	0.74	45.45		
zHUM02-21-4	zircon	Schist	81.75845	30.01709	2520	2.39	0.19	639.7	238.5	2.7	694.6	0.37	7.0	7.02	0.78	53.61		
																	2.56	0.70

Reduced (U-Th[Sm])/He Data

Sample	Mineral	Unit / Lithology	Latitude	Longitude	Elevation (m)	Age, Ma	err., Ma	U (ppm)	Th (ppm)	147Sm (ppm)	[U]e	Th/U	He (nmol/g)	mass (ug)	Ft	ESR	Average Age (Ma)	Age err. (Ma)
HUM02-23		***gn***																
zHUM02-23-1	zircon	Leucogranite	81.74409	30.03481	2530	3.80	0.23	1009.0	66.3	2.2	1024.2	0.07	16.2	7.31	0.77	49.74		
zHUM02-23-2	zircon	Leucogranite	81.74409	30.03481	2530	2.47	0.15	225.7	14.2	0.1	229.0	0.06	2.4	7.92	0.79	54.58		
zHUM02-23-3	zircon	Leucogranite	81.74409	30.03481	2530	2.63	0.16	554.7	28.5	0.7	561.3	0.05	6.5	12.95	0.82	65.10		
zHUM02-23-4	zircon	Leucogranite	81.74409	30.03481	2530	3.93	0.24	367.7	56.2	0.5	380.7	0.15	6.7	17.19	0.83	71.06		
zHUM02-23-5	zircon	Leucogranite	81.74409	30.03481	2530	2.68	0.16	319.7	38.5	0.2	328.5	0.12	3.9	13.36	0.82	65.09		
																	3.10	0.95
Central Transect																		
HUM02-66		***ghs***																
zHUM02-66-1	zircon	Schist	81.33666	30.15413	3680	5.81	0.46	278.1	12.8	0.1	281.1	0.05	7.4	19.24	0.84	72.68		
zHUM02-66-2	zircon	Schist	81.33666	30.15413	3680	5.43	0.43	185.6	31.2	0.6	192.8	0.17	4.8	25.72	0.85	80.51		
zHUM02-66-3	zircon	Schist	81.33666	30.15413	3680	5.37	0.43	490.2	89.4	0.5	510.8	0.18	12.6	31.37	0.85	80.63		
																	5.54	0.68
HUM02-70		***ghs***																
zHUM02-70-1	zircon	Leucogranite	81.36641	30.16128	3750	4.29	0.34	1683.0	103.3	0.5	1706.8	0.06	31.5	7.92	0.80	57.09		
zHUM02-70-3	zircon	Leucogranite	81.36641	30.16128	3750	4.59	0.37	2434.9	126.5	0.6	2464.1	0.05	45.0	3.59	0.74	43.03		
zHUM02-70-5	zircon	Leucogranite	81.36641	30.16128	3750	4.16	0.33	502.6	33.0	0.2	510.2	0.07	9.4	12.85	0.83	66.53		
																	4.35	0.83
HUM02-71		***ghs***																
zHUM02-71-1	zircon	Schist	81.37155	30.15967	3830	4.96	0.40	244.7	52.3	0.4	256.7	0.21	5.1	4.11	0.74	44.47		
zHUM02-71-2	zircon	Schist	81.37155	30.15967	3830	5.46	0.44	269.1	30.5	0.2	276.1	0.11	6.2	5.30	0.77	48.63		
zHUM02-71-3	zircon	Schist	81.37155	30.15967	3830	5.74	0.46	317.0	87.1	0.6	337.0	0.27	7.8	4.60	0.75	46.19		
																	5.39	0.83
HUM02-72		***gn***																
zHUM02-72-1	zircon	Gneiss	81.44885	30.19787	3840	5.07	0.41	178.4	43.7	0.2	188.5	0.25	4.3	16.40	0.84	71.94		
zHUM02-72-3	zircon	Gneiss	81.44885	30.19787	3840	4.79	0.38	204.9	36.0	0.6	213.2	0.18	4.3	6.81	0.78	52.80		
zHUM02-72-4	zircon	Gneiss	81.44885	30.19787	3840	4.31	0.34	128.8	20.3	0.3	133.5	0.16	2.4	5.97	0.77	50.18		
zHUM02-72-5	zircon	Gneiss	81.44885	30.19787	3840	4.10	0.33	231.0	18.9	0.2	235.3	0.08	4.0	5.54	0.77	48.75		
zHUM02-72-6	zircon	Gneiss	81.44885	30.19787	3840	4.87	0.39	137.2	24.0	0.2	142.7	0.18	3.1	11.40	0.82	65.42		
zHUM02-72-7	zircon	Gneiss	81.44885	30.19787	3840	4.34	0.35	112.8	9.5	0.1	115.0	0.08	2.2	9.30	0.81	59.97		
zHUM02-72-8	zircon	Gneiss	81.44885	30.19787	3840	4.70	0.38	97.1	14.8	0.2	100.5	0.15	2.0	6.99	0.79	54.73		
																	4.60	0.72
HUM02-74		***gn***																
zHUM02-74-1	zircon	Leucogranite	81.47203	30.20360	3580	5.16	0.41	4423.5	197.6	1.5	4469.0	0.04	80.8	2.22	0.65	30.98		
zHUM02-74-2	zircon	Leucogranite	81.47203	30.20360	3580	4.79	0.38	4346.2	139.0	0.8	4378.2	0.03	79.7	2.75	0.71	37.55		
zHUM02-74-3	zircon	Leucogranite	81.47203	30.20360	3580	5.64	0.45	8857.5	274.0	1.6	8920.6	0.03	210.8	9.01	0.78	51.36		
																	5.19	0.84
HUM02-75		***gn***																
zHUM02-75-1	zircon	Schist	81.48165	30.20678	3640	6.97	0.56	1372.1	310.0	0.9	1443.4	0.23	42.7	7.80	0.79	54.78		
zHUM02-75-2	zircon	Schist	81.48165	30.20678	3640	4.67	0.37	251.4	69.3	0.6	267.3	0.28	5.2	6.87	0.78	51.93		
zHUM02-75-3	zircon	Schist	81.48165	30.20678	3640	5.94	0.48	522.9	76.5	0.4	540.5	0.15	13.6	7.13	0.78	53.62		
zHUM02-75-4	zircon	Schist	81.48165	30.20678	3640	5.00	0.40	308.2	106.4	0.5	332.7	0.35	6.7	4.45	0.74	44.59		
zHUM02-75-5	zircon	Schist	81.48165	30.20678	3640	5.98	0.48	562.4	127.7	0.5	591.9	0.23	14.2	4.03	0.74	44.43		
																	5.71	1.36

Reduced (U-Th[Sm])/He Data

Sample	Mineral	Unit / Lithology	Latitude	Longitude	Elevation (m)	Age, Ma	err., Ma	U (ppm)	Th (ppm)	147Sm (ppm)	[U]e	Th/U	He (nmol/g)	mass (ug)	Ft	ESR	Average Age (Ma)	Age err. (Ma)
HUM02-76		***ghs***																
zHUM02-76-1	zircon	Schist	81.49373	30.21022	3730	5.71	0.46	260.4	68.9	0.4	276.2	0.26	6.8	10.35	0.80	58.46		
zHUM02-76-2	zircon	Schist	81.49373	30.21022	3730	6.16	0.49	431.2	113.0	1.0	457.3	0.26	12.6	14.78	0.83	68.02		
zHUM02-76-3	zircon	Schist	81.49373	30.21022	3730	5.66	0.45	262.3	37.1	0.5	270.9	0.14	6.5	8.16	0.79	53.75		
zHUM02-76-4	zircon	Schist	81.49373	30.21022	3730	5.79	0.46	332.6	77.0	0.7	350.3	0.23	8.4	6.52	0.77	49.18		
zHUM02-76-5	zircon	Schist	81.49373	30.21022	3730	6.17	0.49	414.7	89.4	0.5	435.3	0.22	11.1	6.69	0.77	49.74		
																	5.90	0.72
HUM02-77		***mig***																
zHUM02-77-1	zircon	Leucogranite	81.51873	30.21959	3800	6.78	0.54	1166.3	86.8	0.9	1186.3	0.07	32.2	4.15	0.74	44.04		
zHUM02-77-3	zircon	Leucogranite	81.51873	30.21959	3800	6.56	0.52	1032.0	83.4	0.9	1051.3	0.08	28.4	5.13	0.76	48.44		
zHUM02-77-4	zircon	Leucogranite	81.51873	30.21959	3800	5.50	0.44	166.9	19.8	0.4	171.5	0.12	4.2	16.03	0.82	64.05		
zHUM02-77-7	zircon	Leucogranite	81.51873	30.21959	3800	6.10	0.49	268.0	42.5	0.6	277.8	0.16	7.5	21.56	0.82	64.46		
																	6.23	1.06
HUM02-79		***mig***																
zHUM02-79-1	zircon	Migmatite	81.56385	30.23281	3850	6.51	0.52	135.6	72.5	0.5	152.3	0.53	4.0	5.28	0.74	45.15		
zHUM02-79-2	zircon	Migmatite	81.56385	30.23281	3850	6.17	0.49	429.2	45.0	0.5	439.5	0.10	10.9	4.11	0.74	43.97		
zHUM02-79-3	zircon	Migmatite	81.56385	30.23281	3850	7.41	0.59	312.0	56.5	0.4	325.0	0.18	9.6	4.52	0.74	44.10		
zHUM02-79-4	zircon	Migmatite	81.56385	30.23281	3850	6.39	0.51	187.4	25.2	0.2	193.2	0.13	4.8	3.72	0.73	41.04		
zHUM02-79-5	zircon	Migmatite	81.56385	30.23281	3850	6.07	0.49	253.0	46.8	0.5	263.7	0.18	6.3	3.47	0.73	42.16		
																	6.51	1.05
HUM02-80		***mig***																
zHUM02-80-1	zircon	Gneiss	81.59305	30.23931	3970	7.69	0.62	143.6	41.6	0.6	153.2	0.29	5.0	8.03	0.79	55.74		
zHUM02-80-2	zircon	Gneiss	81.59305	30.23931	3970	8.69	0.70	522.5	138.0	0.8	554.2	0.26	20.4	7.93	0.78	53.86		
zHUM02-80-3	zircon	Gneiss	81.59305	30.23931	3970	8.12	0.65	514.9	136.2	0.5	546.3	0.26	17.8	4.74	0.75	45.07		
zHUM02-80-4	zircon	Gneiss	81.59305	30.23931	3970	7.51	0.60	265.1	104.3	0.3	289.1	0.39	9.6	14.48	0.82	65.95		
zHUM02-80-5	zircon	Gneiss	81.59305	30.23931	3970	8.74	0.70	190.5	25.0	0.2	196.3	0.13	8.0	33.20	0.86	86.21		
zHUM02-80-6	zircon	Gneiss	81.59305	30.23931	3970	8.38	0.67	77.9	33.8	0.3	85.7	0.43	3.2	24.06	0.84	73.96		
zHUM02-80-7	zircon	Gneiss	81.59305	30.23931	3970	6.92	0.55	54.5	14.0	0.2	57.7	0.26	1.8	25.40	0.86	82.36		
																	8.01	1.31
Northern Transect																		
PK61307-2		***mig***																
zPK61307-2-1	zircon	Gneiss	81.44437	30.43082	5500	7.10	0.43	222.2	50.5	0.7	233.8	0.23	7.7	32.91	0.86	82.18		
zPK61307-2-2	zircon	Gneiss	81.44437	30.43082	5500	6.54	0.39	329.9	92.0	7.2	351.2	0.28	9.9	11.57	0.80	59.15		
zPK61307-2-3	zircon	Gneiss	81.44437	30.43082	5500	8.02	0.48	212.2	63.5	0.7	226.9	0.30	7.9	13.54	0.81	61.51		
																	7.22	1.18
PK61407-2		***gn***																
zPK61407-2-1	zircon	Leucogranite	81.46428	30.44253	5670	5.96	0.36	178.7	31.2	0.3	185.9	0.17	4.8	10.36	0.81	61.91		
zPK61407-2-2	zircon	Leucogranite	81.46428	30.44253	5670	6.00	0.36	236.5	76.4	0.5	254.1	0.32	6.8	16.21	0.83	68.26		
zPK61407-2-3	zircon	Leucogranite	81.46428	30.44253	5670	6.62	0.40	342.3	52.4	0.5	354.3	0.15	9.9	8.07	0.78	53.35		
																	6.19	0.75
PK61507-1B		***gn***																
zPK61507-1B-1	zircon	Metasandstone	81.44890	30.48333	5200	5.24	0.31	93.5	34.0	0.3	101.3	0.36	2.1	4.74	0.74	45.07		
zPK61507-1B-2	zircon	Metasandstone	81.44890	30.48333	5200	7.07	0.42	449.0	64.6	0.7	463.8	0.14	12.0	2.72	0.68	34.64		
zPK61507-1B-3	zircon	Metasandstone	81.44890	30.48333	5200	6.08	0.36	297.3	247.3	0.6	354.2	0.83	7.6	1.81	0.65	32.37		
																	6.13	0.84

Table 1:

Zircon (U-Th)/He data separated into the three transects. Mean sample ages with error are shown on the right. Sample error is derived from the standard lab error (8%) combined with the standard deviation of the sample aliquots. Ft – Alpha ejection correction; ESR – Equivalent Spherical Radius.

Table 2:

PeCube Transect Parameters			
Northern Transect	*Range*	*Units*	*References*
Initiation Age	9.0-18.0	Ma	Murphy et al., 2002
Acceleration Age	0.0-14.0	Ma	
Initial Rate	1.0-12.0	mm/yr	
Post-Acceleration Rate	0.0-12.0	mm/yr	
Central Transect			
Initiation Age	9.0-18.0	Ma	Murphy et al., 2002
Acceleration Age	0.0-14.0	Ma	
Initial Rate	1.0-12.0	mm/yr	
Post-Acceleration Rate	0.0-12.0	mm/yr	
Southern Transect			
Initiation Age	7.0-15.0	Ma	Murphy and Copeland., 2005
Acceleration Age	0.0-14.0	Ma	
Initial Rate	1.0-12.0	mm/yr	
Post-Acceleration Rate	0.0-12.0	mm/yr	
PeCube Model Parameters			
Fault Dip	30	Degrees	Murphy et al., 2002; Murphy and Copeland, 2005
Moho Temperature	800	°C	Nabelek et al., 2010
Radiogenic Heating	10	°C/Myr	Faccenda et al., 2008
Model Thickness	65	km	Nabelek et al., 2009; Chen et al., 2010
Skipping Facotor	15		

Table 2:

Table of variables tested in each of the three transects and the parameters used in the basic PeCube model.

Table 3:

PeCube Modeling Results	Mean Fault Slip Rate	Initiation Age	Initiation Rate	Acceleration Age	Post-Acceleration Rate	Total Fault Slip
Units	mm/yr	Ma	mm/yr	Ma	mm/yr	km
Northern Transect	4.5±1.1	14-9	8-10	6	1-3	35.0
Central Transect	3.8±1.2	14-11	3-5	5-4	3	40.0
Southern Transect	3.2±1.3	15-8	1-3	7-4	1-3	20-35
Northern Transect Best Fit	5.0±0.9	14-11	8-11	6	1-2	58-69
Central Transect Best Fit	3.3±0.6	14-11	2-4	13-11	3	40-46
Southern Transect Best Fit	2.7±1.1 / 3.8±1.0	15-8	1-2	6-3	2-4	20-35 / 25-65

Table 3:

Table of modeling results and best fit modeling results.

Table 4:

Fault	Location	Timing	Methods	Rates (mm/yr)	Source	Symbol
GMD	Northern Transect	12 - 6 / 6 - 0 Ma	(U-Th)/He	5.9 - 4.1	This study	NT
GMD	Central Transect	14 - 0 Ma	(U-Th)/He	3.9 - 2.7	This study	CT
GMD	Southern Transect	11 - 0 Ma	(U/Th)/He	1.6 - 4.8	This study	ST
KF	Northern	23 - 0 Ma		6 - 12	Robinson et al., [2009]	R9
KF	Northern	15 - 0 Ma	U-Pb	2.7 - 10.2	Phillips et al., [2004]	P4
KF	Northern	15 - 0 Ma	U-Pb	3 - 10	Rutter et al., [2007]	R7
KF	Central	23 - 0 Ma	$^{40}Ar/^{39}Ar$, FT, U-Pb	7 - 13	Lacassin et al., [2004]	L4
KF	Central	23 - 0 Ma	$^{40}Ar/^{39}Ar$, FT, U-Pb	7 - 10	Valli et al., [2007, 2008]	V7
KF	Central	18 - 0 Ma	$^{40}Ar/^{39}Ar$, U-Pb	7.3 - 9.3	Searle et al., [1998]	S98
KF	Central	13 - 0 Ma	$^{40}Ar/^{39}Ar$, U-Pb	7 - 15	Wang et al., [2011]	W11
KF	Central	200 ka	^{10}Be Cosmogenics	6 -11	Chevalier et al., [2005a, 2005b]	CH5
KF	Central	12 ka	^{10}Be Cosmogenics	8 - 10	Chevalier et al., [2011]	CH11
KF	Central	14 ka	^{10}Be Cosmogenics	3 - 5	Brown et al., [2002]	B2
KF	Central	< 10 a	GPS	7 - 15	Banerjee and Burgmann, [2002]	BB2
KF	Central	< 10 a	GPS	3 - 5	Chen et al., [2004]	C4
KF	Central	< 10 a	GPS	0 - 8	Jade et al., [2004, 2010]	J10
KF	Central	< 10 a	GPS	3 - 5.5	Loveless and Meade, [2011]	L11
KF	Central	< 10 a	InSAR	1 - 4	Wright et al., [2004]	W4

* Slip-rate calculated assuming a fault dip of 30°

Fault	Location	Timing	Methods	Rates (mm/yr)	Source	Symbol
KF	Central	< 10 a	InSAR	0 - 8	Wang and Wright, 2012	WW12
KF	Central	< 10 a	GPS	4 - 10	Zhang et al., [2004]	Z4
KF	Southern	13 - 0 Ma	$^{40}Ar/^{39}Ar$	4.0 - 6.0	Murphy et al., [2000]	M0
KF	Southern	12 - 0 Ma	$^{40}Ar/^{39}Ar$, U-Pb	5 - 9	Wang et al., [2009]	W9
KF	Southern	12 - 0 Ma	U-Pb	4.4 - 4.6	Wang et al., [2012]	W12
KF	Southern	< 100 ka	^{10}Be Cosmogenics	5 - 11	Chevalier et al., [2012]	CH12a
GMD	Southern	15 - 0 Ma	$^{40}Ar/^{39}Ar$	1.4 - 4.6	Murphy and Copeland, [2005]	MC5
GMD	Northern / Central	13 - 0 Ma	$^{40}Ar/^{39}Ar$	2.7 - 7.3	Murphy et al., [2002]	M2
GMD	Northern / Central	40 ka	^{10}Be Cosmogenics	*4.0 - 2.6	Chevalier et al., [2012]	CH12b

* Slip-rate calculated assuming a fault dip of 30°

Table 4:

Table of Gurla Mandhata (GMD) and Karakoram fault (KF) slip-rates corresponding to Figure 17. Red text is from this study, blue text is data for the GMD, and the green text is data for the KF.